

Supernova fallback and the emergence of a black hole

Luca Zampieri ¹, Monica Colpi ², Stuart L. Shapiro ^{1,3} and Ira Wasserman ⁴

ABSTRACT

We present the first fully relativistic investigation of matter fallback in a supernova. We investigate spherically symmetric supernova fallback using a relativistic radiation hydrodynamics Lagrangian code that handles radiation transport in all regimes. Our goal is to answer the fundamental question: did SN1987A produce a black hole and, if so, when will the hole become detectable? We compute the light curve, assuming that a black hole has been formed during the explosion, and compare it with the observations. Our preliminary calculations lack radioactive energy input and adopt a very simple chemical composition (pure hydrogen). As a result, our computed models cannot fit the observed data of SN1987A in detail. Nevertheless, we can show that, during the first hours, the accretion flow is self-regulated and the accretion luminosity stays very close to the Eddington limit. The light curve is completely dominated, during the first few weeks, by the emission of the stellar envelope thermal energy, and resembles that obtained in “standard” supernova theory. Only long after hydrogen recombination takes place is there even a chance to actually detect radiation from the accreting black hole above the emission of the expanding envelope. The presence of a black hole is thus not inconsistent with observations to date. Because of the exponential decay of the ⁴⁴Ti radioactive heating rate, the date of the emergence of the black hole is not very sensitive to the actual parameters of the models and turns out to be about 1000 years. The bulk of the emission then is expected to be in the visible band, but will be unobservable with present instrumentation. We discuss the implications of our results in connection with the possible emergence of a black hole in other supernovae.

Subject headings: Accretion, accretion disks — hydrodynamics — methods: numerical — radiative transfer — relativity — supernovae: individual (SN1987A)

1. Introduction

On the 23rd of February 1987, Shelton and Jones announced the discovery of a supernova in the Large Magellanic Cloud, SN1987A (Kunkel *et al.* 1987). Historically, this was the brightest supernova observed after that recorded by Kepler in 1604 (SN1604). It was also the first supernova to be observed in every band of the electromagnetic spectrum and the first detected through its initial burst of neutrinos. Its relatively close distance (~ 50 Kpc) has offered a unique opportunity to observe a supernova in great

¹Department of Physics, Loomis Laboratory of Physics, University of Illinois at Urbana-Champaign, 1110 West Green Street, Urbana, IL 61801-3080

²Dipartimento di Fisica, Università degli Studi di Milano, Via Celoria 16, I-20133 Milano, Italy

³Department of Astronomy and National Center for Supercomputing Applications, University of Illinois at Urbana-Champaign, Urbana, IL 61801

⁴Center for Radiophysics and Space Research, Cornell University, Ithaca, NY 14853

detail and with a variety of detection techniques. [For extensive reviews on SN1987A see e.g. Arnett *et al.* (1989), McCray (1993) and references therein.] Since its appearance, SN1987A has confirmed many aspects of the theory of type II supernovae (see e.g. Dar 1997). As predicted, most of the energy ($\sim 10^{53}$ erg) was released in ~ 10 s by the cooling of the proton-neutron star and was radiated in form of neutrinos, detected by the Mont Blanc, Kamiokande, IMB and Baksan underground detectors. The strong shock produced by the core bounce heated and pushed outwards the stellar envelope, which subsequently emitted its internal energy as photons: the integrated light emission was $\sim 10^{49}$ erg, while the kinetic energy of the expanding shells was $\sim 10^{51}$ erg. The light curve can be fitted quite well by the “standard” type II supernova theory (see e.g. Woosley 1988; Arnett 1996). After the emergence of the shock wave, the emission is dominated by the diffusion luminosity of the expanding stellar envelope during the first 30–40 days. At ~ 40 days, the hydrogen envelope starts to recombine and a large amount of internal energy is released by the inward motion of the recombination front. After most of the envelope has recombined at day ~ 160 , the light curve starts to be dominated by the radioactive decay of heavy elements synthesized during the explosion. Some predictions of the “standard” theory were not confirmed and a number of key issues remain to be answered, such as the nature of the supernova progenitor, the explosion mechanism and, perhaps most important, the nature of the compact remnant left over after the explosion.

Stellar evolution calculations show that stars with a main sequence mass in the range 8–19 M_{\odot} finish their lives with a compact core of $\sim 1.4M_{\odot}$. As shown by Woosley & Weaver (1995), for these stars the amount of material that falls back toward the core in the aftermath of its collapse is negligible, so it is likely that they give birth to neutron stars. Stars with main sequence mass larger than $M_c \sim 25$ –30 M_{\odot} have more massive cores ($\simeq 2M_{\odot}$) and undergo accretion of a significant amount of matter, so that the remnant mass left over after the explosion is larger than $3M_{\odot}$, probably leading to the formation of a black hole. The value of M_c is somewhat uncertain and depends quite sensitively on the mass loss prior to the explosion (reduced core mass) and on the explosion energy (amount of fall back). The fate of stars in the intermediate range 19–25 M_{\odot} is far less obvious. At the end of their evolution, they have core masses around 1.6–1.8 M_{\odot} and a variable amount of matter, 0.1–0.3 M_{\odot} may fall back because of the hydrodynamic interaction of the outgoing supernova shock with the expanding envelope (Woosley & Weaver 1995). Typically, these stars leave a central compact remnant of 1.7–2.1 M_{\odot} (baryonic mass). Then their fate depends critically on the equation of state at nuclear matter densities that fixes the maximum mass M_{crit} above which no stable neutron star configuration can exist. Adopting the parametrization of the nuclear matter equation of state by Lattimer & Swesty (1991), M_{crit} turns out to be $M_{crit} \lesssim 2.5M_{\odot}$ (gravitational mass). In this case, it would be unlikely that these stars could form a black hole. However, Thorsson, Prakash & Lattimer (1994) have proposed a much softer equation of state as a consequence of K^- condensation. They find a maximum mass $M_{crit} \simeq 1.5M_{\odot}$ (gravitational mass). Recently, modern models of nuclear forces and accurate Monte Carlo modeling of nucleon interactions indicate that $M_{crit} = 1.8$ –2.2 M_{\odot} (Pandharipande 1997). Based on the findings of Thorsson, Prakash & Lattimer (1994), Brown & Bethe (1994) and Woosley & Timmes (1996) have proposed different scenarios that may lead to the formation of a black hole after the explosion of a 19–25 M_{\odot} star. According to Brown & Bethe (1994), after core bounce a proton-neutron star would form that could remain stable for about ~ 12 s (just the time necessary to release its internal energy in form of neutrinos) and then would collapse to a black hole, as early suggested by Wilson *et al.* (1986) and Woosley & Weaver (1986). Woosley & Timmes (1996) point out that the formation of a black hole could be driven by the matter which falls back in the first few hours after the explosion, as already emphasized by Colgate (1971, 1988) and Chevalier (1989).

Interestingly, the mass of the progenitor of SN1987A ($M = 18$ –21 M_{\odot}) falls in the range of masses where the outcome of core collapse is uncertain. So, from a theoretical point of view, we do not know if a

neutron star or a black hole has been formed during the explosion. The main uncertainties are the value of the critical mass above which no stable neutron star can exist and the amount of matter that falls back during the explosion. If there was no fallback in SN1987A, the emission from a radio pulsar most probably would not be detectable directly for a very long time, unless there are holes in the outflow. Observations also rule out the presence of any optical pulsar. The energy deposition from a pulsar could alter the light curve, though; observations to date limit any energy input from a pulsar to be lower than the contribution from radioactive decay ($\sim 10^{36}$ erg s $^{-1}$, implying $B/P^2 \sim 10^{14}$ G s $^{-2}$ for magnetic dipole emission by a pulsar with field strength B and rotation period P). However, high energy X-rays from a pulsar radiating a hard spectrum should have become observable in a few months (McCray, Shull and Sutherland 1987) although the 1–3 keV thermal X-ray emission from the cooling of a neutron star would be attenuated for about 100 yr (Chernoff, Shapiro and Wasserman 1989). Such hard X-rays were never observed.

If a compact object of any kind is present, it is probably accreting from the progenitor stellar material, since the inner part of the ejecta have velocity smaller than the escape velocity. During the first phases after the explosion, the accretion rate should be as high as 10^8 in units of the Eddington accretion rate (Chevalier 1989). On the other hand, as mentioned above, the bolometric light curve observed to date (ten years after the explosion) can be explained by the “standard” theory of Type II supernovae and does not show any feature related to the possible presence of a central accreting compact object. Using analytic and numerical methods, Chevalier (1989) and Houck & Chevalier (1991) have investigated the problem of fall back onto a neutron star and found that, for radiation pressure–limited accretion, the luminosity emitted after 3–4 years should approach the Eddington value, $L_{Edd} \sim 10^{38}$ erg s $^{-1}$ for gas opacity dominated by electron (Thomson) scattering. Since at ~ 1500 days the bolometric luminosity of SN1987A was $\sim 10^{37}$ erg s $^{-1}$, they argue that either the accreting envelope becomes dynamically unstable or SN1987A contains a black hole. On the other hand, Chen & Colgate (1995) noted that, at the typical temperature and density of the ejecta after few years, the opacity in the accreting gas enriched of heavy elements is much larger than the Thomson opacity. So, they conclude that a neutron star accreting at the actual (non–Thomson) Eddington limit may be present. Furthermore, if the value of the critical mass falls in the range 1.8–2.2 M_{\odot} , as seems to be indicated by recent developments in the nuclear many–body theory (Pandharipande 1997), it appears that the amount of fallback is a key element in determining whether or not a stellar black hole has formed. SN1987A may or may not harbor a black hole but observations alone have not resolved this issue yet. It is therefore important to determine what extra luminosity an accreting central component would produce and when its presence might be discernible. The amount of fallback depends on the main parameters of the explosion while the visibility of the remnant on the detailed hydrodynamical evolution of the flow and of the radiation field.

This is the first of a series of papers in which we address a number of relevant questions: can we infer from the light curve whether a stellar black hole has formed in the aftermath of a supernova explosion? Did SN1987A produce a neutron star or a black hole? We will consider these issues by assuming that either a black hole or a neutron star has formed and then will compute the resulting light curve varying the main parameters of the explosion. Our focus will be to isolate the contribution from the central compact object.

In this paper we present the first self–consistent, fully relativistic investigation of supernova fallback in presence of a black hole. It is the relativistic generalization of the work by Colpi, Shapiro & Wasserman (1996, hereafter CSW) in which the hydrodynamical properties of a fluid accreting onto a central remnant from an initially expanding cloud were first explored. Here, we include self-consistently the transfer of radiation. Due to the complexity of the problem we will not attempt to investigate a model with realistic chemical composition (that will be presented in a forthcoming paper) but, instead, we will consider a

number of simpler preliminary scenarios to guide our understanding. We will show that, during the first hours, the accretion flow is self-regulated and the accretion luminosity stays very close to the Eddington limit. However, during the first few weeks the light curve is completely dominated by the emission of the stellar envelope internal energy, giving a light curve that resembles that obtained in the “standard” supernova theory. Although in this paper we apply our calculation specifically to SN1987A, our results have general validity and can be used to study the light curve and the observational signatures of black holes in other supernovae.

We have investigated spherically symmetric supernova fallback using a general-relativistic, radiation hydrodynamic Lagrangian code. Our code can handle the transfer of radiation from the first phases immediately after the supernova explosion (when photons diffuse through a high temperature, expanding cloud) to the late evolutionary stages (when the hydrogen envelope has recombined and most of the ejecta are transparent). The main challenge we have confronted is the enormous dynamic range in the relevant physical timescales entering the problem. To this end, we have implemented a multiple timestep procedure that allows us to integrate different radial regions at different rates (a primitive “temporal adaptive mesh”). This technique enables us to speed up the calculation by almost an order of magnitude.

The plan of the paper is the following: in Section 2 we present the general relativistic equations of radiation hydrodynamics used in the calculation. The finite difference form of these equations is presented in the Appendix. Section 3 describes the numerical method used to solve the equations of radiation hydrodynamics and the boundary conditions adopted. In Section 4 we present in detail the multiple timestep procedure employed in our calculation. Section 5 illustrates the set up of the initial conditions. In Section 6 we present the numerical results for various simplified examples and test cases. Section 7 is devoted to the semi-analytic calculation of the late-time light curve. Finally Section 8 contains a discussion of our preliminary results in connection with SN1987A and with the diagnosis of black holes in supernova explosions.

2. Equations

In this section we present the equations of relativistic radiation hydrodynamics in spherical symmetry for a self-gravitating matter fluid which is interacting with radiation [for a review of the derivation of these equations see Zampieri 1995 and Zampieri, Miller & Turolla 1996]. All the equations will be written in the frame comoving with the fluid flow. The 4-velocity of an element of fluid u^α will be evaluated in the Eulerian frame, defined as the reference frame at rest with respect to the background (spherically symmetric) metric. In this frame, the areal radius r is taken to be the independent radial (Schwarzschild) coordinate. We now introduce the spherically symmetric, comoving-frame line element

$$ds^2 = -a^2 dt^2 + b^2 d\mu^2 + r^2 (d\theta^2 + \sin^2 \theta d\varphi^2) , \quad (1)$$

where t and μ are the Lagrangian time and the comoving radial coordinate (taken to be the rest mass contained within a comoving spherical shell) and a and b are two functions of t and μ which need to be computed from the Einstein field equations. Here and throughout we adopt geometrized units and set $c = G = 1$. Using the line element (1), the complete system of radiation hydrodynamics equations in the frame comoving with the flow along with the Einstein field equations can be cast into the form (Rezzolla & Miller 1994; Zampieri, Miller & Turolla 1996)

$$e_{,t} - h\rho_{,t} + as_0 = 0 \quad (2)$$

$$u_{,t} + a \left[\frac{\Gamma}{b} \left(\frac{p_{,\mu} + bs_1}{\rho h} \right) + 4\pi r \left(p + \frac{1}{3}w_0 + w_2 \right) + \frac{M}{r^2} \right] = 0 \quad (3)$$

$$\frac{(\rho r^2)_{,t}}{\rho r^2} + a \left(\frac{u_{,\mu} - 4\pi b r w_1}{r_{,\mu}} \right) = 0 \quad (4)$$

$$b = \frac{1}{4\pi r^2 \rho} \quad (5)$$

$$\frac{(ah)_{,\mu}}{ah} + \frac{h\rho_{,\mu} - e_{,\mu} + bs_1}{h\rho} = 0 \quad (6)$$

$$M_{,\mu} = 4\pi r^2 r_{,\mu} \left(e + w_0 + \frac{u}{\Gamma} w_1 \right) \quad (7)$$

where

$$u = \frac{r_{,t}}{a} \quad (8)$$

is the radial component of the fluid 4-velocity measured in the Eulerian frame, $\Gamma \equiv r_{,\mu}/b = (1+u^2-2M/r)^{1/2}$, M represents the effective gravitational mass-energy (for black hole + gas + radiation) contained within radius r and ρ , e , p and $h = (e+p)/\rho$ are the rest-mass density, total mass-energy density, pressure and enthalpy of the gas flow, respectively, as measured in the comoving frame. Here s_0 and s_1 are the radial PSTF moments of the source function that account for energy and momentum exchange between the fluid flow and the radiation field. Their actual forms depend on the radiative processes considered (see below). Finally, w_0 , w_1 and w_2 denote the first three radial PSTF moments of the specific intensity I of the radiation field, measured in the comoving frame and given by

$$w_k = 2\pi \frac{k!(2k+1)}{(2k+1)!!} \int IP_k(\hat{\mu}) d\hat{\mu}, \quad (9)$$

where $\hat{\mu}$ is the cosine of the angle between the photon propagation and radial directions and $P^k(\hat{\mu})$ is the Legendre polynomial of order k . In terms of the ‘‘classical’’ moments of the specific intensity J , H and K , we have: $w_0 = 4\pi J$, $w_1 = 4\pi H$, $w_2 = 4\pi(K - J/3)$.

The radiation hydrodynamic equations must be supplemented with the radiation moment equations. In spherical symmetry with the line-element (1), the first two frequency-integrated PSTF moments of the relativistic transfer equation can be written (Zampieri, Miller & Turolla 1996)

$$\frac{1}{b^{4/3} r^{8/3}} \left(w_0 b^{4/3} r^{8/3} \right)_{,t} + \frac{1}{abr^2} (w_1 a^2 r^2)_{,\mu} + \left(\frac{b_{,t}}{b} - \frac{r_{,t}}{r} \right) w_2 - as_0 = 0, \quad (10)$$

$$\frac{1}{b^2 r^2} (w_1 b^2 r^2)_{,t} + \frac{1}{3a^3 b} (w_0 a^4)_{,\mu} + \frac{1}{br^3} (w_2 ar^3)_{,\mu} - as_1 = 0. \quad (11)$$

In equations (10) and (11) w_0 and w_1 have the dimensions of energy density. To close the moment equations, we employ interpolations of the Eddington factors for a spherically symmetric, static atmosphere in radiative equilibrium, that fit the data from Hummer & Rybicki (1971) to within 30%. The expression for the Eddington factor $f = w_2/w_0$ and the Eddington boundary factor $g = w_1(r_{out})/w_0(r_{out})$ are given by

$$f = \left[\frac{2}{3} - 0.59 \left(\frac{r_1}{r_{out}} \right) \right] \frac{1}{1 + 3\tau}, \quad (12)$$

$$g = 1 - 0.423 \left(\frac{r_1}{r_{out}} \right), \quad (13)$$

where τ is the optical depth (see below), r_1 is the radius at which $\tau = 1$ and r_{out} is the outer radial boundary of the flow. Note that $0 \leq f \leq 2/3 - 0.59(r_1/r_{out})$. The use of equations (12) and (13) is not

exact, especially for a moving gas. However, adopting any kind of iterative procedure to calculate the Eddington factors precisely (see e.g. Shapiro 1996) would be too expensive from the computational point of view. Moreover, the error introduced by equations (12) and (13) is certainly not larger than that caused by the use of mean opacities in the source moments (see below) and, hence, is adequate for the present frequency-integrated calculations.

In this paper we will use very simple input physics for the coupled gas equations of state and the source moments. For our simplest models we will adopt a totally ionized hydrogen gas with constant opacity (independent of ρ and T). From the numerical calculations we have found that, during computation, the maximum gas temperature is reached near the horizon and is not larger than $\sim 5 \times 10^8 K$. In our more detailed models we will consider a hydrogen gas with variable degree of ionization, computed using the Saha equation. In a forthcoming paper we will treat a more realistic gas composition. If the electrons are nonrelativistic ($T < 10^9 K$), we have

$$p = [1 + x(T)] \frac{\rho k_B T}{m_p}, \quad (14)$$

$$e = \rho \left\{ 1 + \frac{3}{2} [1 + x(T)] \frac{k_B T}{m_p} - [1 - x(T)] \frac{E_H}{m_p} \right\}, \quad (15)$$

where T is the gas temperature, $E_H = 13.6$ eV is the hydrogen ionization potential and $x(T)$ is the degree of ionization, given by

$$x(T) = \frac{\delta}{1 + \delta}. \quad (16)$$

We assume that all atoms are in their ground state. The function δ is the positive root of the Saha quadratic equation (Rybicki & Lightman 1979)

$$\frac{\delta^2}{1 + \delta} = \frac{m_H}{\rho} \left(\frac{2\pi m_e k_B T}{h^2} \right)^{3/2} e^{-E_H/k_B T}. \quad (17)$$

Equation (17) holds in the “one level atom” limit for hydrogen, i.e. when the temperature is fairly low compared to E_H . Although this is not going to be true for our calculations throughout all the grid, however it is still true that equation (17) will give a large ionization at high temperature. The third term inside the curly brackets in equation (15) accounts for the electrostatic potential energy of bound electrons in the neutral hydrogen atoms. For the opacities, we adopt the interpolation formula by Christy (1966) which, for the range of temperatures and densities considered, fits the hydrogen Rosseland mean opacity k_R to better than 30%:

$$k_R = p_e \left\{ 4.85 \times 10^{-13} \frac{1}{\rho T_4} + T_4^{1/2} \left(\frac{2 \times 10^6}{T_4^4} + 2.1 T_4^6 \right)^{-1} + \left[4.5 T_4^6 + T_4^{-1} \left(\frac{4 \times 10^{-3}}{T_4^4} + \frac{2 \times 10^{-4}}{\rho^{1/4}} \right)^{-1} \right]^{-1} \right\}, \quad (18)$$

where p_e is the electron pressure and $T_4 = T/10^4 K$. The Planck mean opacity k_P has been calculated approximately by subtracting the Thomson scattering contribution (the first term in the curly brackets in equation [18]) from the expression for k_R . This choice follows from the fact that a very accurate evaluation of k_P is not critically important since the transition of the ejecta from optically thick to thin is governed entirely by the recombination process. Furthermore, no detailed analytic interpolation of the Planck mean opacity in the range of temperature and density of interest here can be found in literature and

numerical interpolation from accurate tabulated opacities would be too expensive in the present preliminary calculation. Using the Kirchhoff law, the first two radial moments of the source function s_0 and s_1 can be written

$$s_0 = \rho(k_P B - k_0 w_0), \quad (19)$$

$$s_1 = -\rho k_1 w_1, \quad (20)$$

where $B = a_R T^4$ (a_R is the blackbody radiation constant) and k_0 and k_1 are the absorption and flux mean opacities. Since in the present frequency-integrated calculation the actual spectral distribution of w_0 and w_1 is not known, we use k_P and k_R in place of k_0 and k_1 , respectively. Finally, the optical depth τ at radius r is defined by

$$\tau = \int_r^\infty k_R \rho dr. \quad (21)$$

3. Numerical method and boundary conditions

The numerical code used to solve the equations of radiation hydrodynamics and the radiation moment equations presented in the previous section is based on a Lagrangian finite difference scheme with a standard Lagrangian organization of the grid (see the Appendix; see also Zampieri, Miller & Turolla 1996). The spatial and time centering of the variables ensures second order accuracy both in space and time. As far as the spatial centering is concerned, ρ , $B = a_R T^4$, w_0 and a are evaluated at mid-zones, while r , M , u and w_1 are evaluated at zone boundaries. To have second-order accuracy in time, u and w_1 are both evaluated at an intermediate time level (time-shifted). Because of the way in which variables are centered, the code is semi-implicit. This feature helps preserve stability (see e.g. Mihalas & Mihalas 1984; Shapiro 1996). The full set of equations in finite difference form is written in the Appendix.

The time step is controlled by the Courant condition for stability and by additional constraints on the fractional variation of the variables ($\leq 10\%$). The Courant condition reads

$$a \Gamma v_c \frac{\Delta t}{\Delta r} < 1, \quad (22)$$

where $v_c = (f + 1/3)^{1/2}$ is the characteristic speed of radiation in the Lagrangian frame (the fastest characteristic speed on the grid in the present problem). The grid in Lagrangian mass μ is usually divided into $j_{max} = 200$ zones. A constant fractional increment in grid spacing between successive zones α is used. It is calculated from the equation

$$\mu_{j_{max}} = \mu_{j_{min}} + \sum_{j=j_{min}}^{j_{max}-1} \Delta \mu_{j+1/2}, \quad (23)$$

where $\mu_{j_{min}}$ is the inner boundary, $\mu_{j_{max}}$ is the outer boundary (fixed for the conservation of the total envelope mass) and $\Delta \mu_{j+1/2} \equiv \mu_{j+1} - \mu_j = \alpha \Delta \mu_{j-1/2}$. At the beginning of the calculation $\mu_{j_{min}} = 0$. The mass contained within the first shell $\Delta \mu_{1/2}$ is fixed by the requirement that the radial spacing between the first two shells is 30% of $r_{j_{min}}$. Equation (23) can be written as a polynomial of order j_{max} in α and has been solved using the Newton-Raphson method. Whenever the inner edge of the innermost zone crosses the inner boundary in radius r_{in} , it is removed from the calculation and a regridding of all the variables is performed. During computation, the actual inner boundary in mass changes according to: $\mu_{j_{min}} = \mu_{j_{min}+l}$, where l is the number of zones that have crossed r_{in} . The fractional increment α is computed solving

equation (23) with the new value of $\mu_{j_{min}}$. All the variables are then interpolated on the new grid. The regridding procedure makes use of a local cubic interpolation that, for uniform spacing, reduces to a local fourth-order Lagrangian interpolation. Performing systematic regriddings is necessary both to minimize the number of grid points and to preserve the spatial resolution with time.

Once the finite difference representation has been introduced, equations (3), (4), (6), (7) and (8) can be solved explicitly (algebraically) for u , ρ , a , M and r , respectively (see Appendix). Where necessary, linear interpolation and extrapolation in time were used to obtain the values of quantities at suitable time levels. Using equation (20) with $k_1 = k_R$, equation (11) is rewritten in the following form

$$\frac{(w_1)_{,t}}{w_1} = -ak_R\rho - 2\left(\frac{b_{,t}}{b} + \frac{r_{,t}}{r}\right) - \frac{a}{w_1} \left[\frac{1}{3a^4b}(w_0a^4)_{,\mu} + \frac{1}{abr^3}(fw_0ar^3)_{,\mu} \right] \quad (24)$$

and solved (algebraically) for w_1 at level $n + 1/2$. The quantity w_2 is expressed using the closure relation $w_2 = fw_0$ with f being defined as in equation (12). Again, where necessary, variables on the right hand side have been interpolated or extrapolated at the correct time level (see Appendix). The energy equation (2) and the 0-th moment equation (10) form a strongly coupled, nonlinear system of equations. Using equations (19) with $k_0 = k_P$, they can be cast into the form

$$\epsilon_{,t} + ak_P(B - w_0) + p\left(\frac{1}{\rho}\right)_{,t} = 0, \quad (25)$$

$$(w_0)_{,t} - ak_P\rho(B - w_0) + \left[\frac{4}{3}\left(\frac{b_{,t}}{b} + 2\frac{r_{,t}}{r}\right) + \left(\frac{b_{,t}}{b} - \frac{r_{,t}}{r}\right)f\right]w_0 + \frac{1}{abr^2}(w_1a^2r^2)_{,\mu} = 0, \quad (26)$$

where $\epsilon = (e - \rho)/\rho$ is the internal energy per unit mass. They have been solved for B and w_0 at the new time level $n + 1$ using the Newton-Raphson method for nonlinear systems of equations.

As far as the boundary conditions are concerned, the time slice at constant t is a characteristic direction for equations (6) and (7). At the outer boundary we put

$$a = 1 \quad \mu = \mu_{j_{max}}. \quad (27)$$

Equation (27) corresponds to synchronizing the coordinate time with the proper time of a comoving observer at the outer edge of the grid. The inner boundary is chosen away from the origin to avoid the black hole singularity. There we set

$$M = M_0 \quad \mu = \mu_{j_{min}}, \quad (28)$$

where M_0 is the effective mass contained within the inner boundary. At $t = 0$ this is taken to be equal to the initial black hole mass M_{bh} . In the limit appropriate here where the infalling fluid at $\mu_{j_{min}}$ is highly supersonic with negligible thermal and radiation back pressure, the gas behaves like dust. In this case, as time increases, we know that the effective mass M increases at the rate at which baryons (i.e. rest mass) cross into r_{in} . Once they cross, they are removed from the calculation. The boundary conditions for the continuity and Euler equations are

$$u_{,t} + \frac{aM}{r^2} = 0 \quad \mu = \mu_{j_{min}}, \quad (29)$$

$$u_{,t} = 0 \quad \mu = \mu_{j_{max}}. \quad (30)$$

Equation (29) corresponds to assuming that pressure gradients and radiative forces can be neglected at the inner boundary and that the free-fall is achieved near to $\mu = \mu_{j_{min}}$. This turns out to be correct if the inner

boundary radius r_{in} is sufficiently smaller than the accretion radius ($r_a = GM_{bh}/c_s^2$). During the initial evolutionary phases, in some of our computed models radiative forces are very important and affect the flow dynamics. However, in the innermost part of the accreting region the luminosity is always sub-Eddington (see Section 6). Thus, if the inner boundary is sufficiently far in, at $\mu = \mu_{j_{min}}$ the gas is moving in near free-fall. The condition at $\mu = \mu_{j_{max}}$ follows from the requirement of free expansion. It is correct as long as the motion of the gas near the outer boundary is supersonic and both radiative and gravitational forces have little influence on the outflow (see e.g. Arnett 1980). The inner boundary condition at $\mu = \mu_{j_{min}}$ for w_1 is a five-point Lagrangian extrapolation in r along the time slice at constant t . To impose the boundary condition at the outer edge of the grid we apply equation (24) across the half-zone from $j_{max} - 1/2$ to j_{max} , substituting $(w_1)_{j_{max}} = g(w_0)_{j_{max}}$ for $(w_0)_{j_{max}}$ in the gradients with respect to μ (see e.g. Mihalas & Mihalas 1984; Shapiro 1996). The closure boundary factor g is given by equation (13).

As already mentioned, the evolutionary times for the present problem are very long in comparison with the timescales involved in the calculation. For this reason we developed a multiple timestep procedure to speed up the calculation, discussed in the next section.

4. Multiple timestep procedure

A situation often encountered in the numerical solution of time-dependent problems is the need to integrate the equations over a very wide range of length scales and corresponding timescales. Frequently, the relevant timescales vary monotonically along the grid. In these situations, integrating every cycle over all of the mesh with the smallest timestep is an unwanted waste of computational time (in particular if the number of grid points is large and/or the evolutionary times are very long), since the evolution is unnecessarily slow in some portions of the grid. We have developed an approach, that seems particularly suitable for the present problem. The basic idea of our multiple timestep procedure (MTP) is to decompose the grid into subgrids, each one evolving separately according to its own timestep. The subgrids with larger timesteps are evolved with fewer steps than those with smaller ones. The major challenge here is establishing the communication between neighboring subgrids. Additional complications arise if the grid is staggered in time, so that some variables are evaluated at the full time level (time centered) whereas other variables are evaluated at half time level (time shifted). Finally, if the code performs systematic regriddings over all the grid, the evolution has to be re-synchronized before performing any interpolation. Our code handles all of these difficulties.

4.1. Communication at the boundaries between neighboring subgrids

In the following we assume that the integration domain has been divided into N subgrids. We assume also that the innermost zone ($k = 1$) has the smallest timestep and that the sequence of subgrids has timesteps monotonically increasing outwards. This assumption is certainly correct in the present case. In deciding the order in which to evolve the various zones, we must consider the subgrid boundaries. Subgrids have boundaries which are in the interior of the integration domain and hence they will need boundary values to close the PDE's. In the Adaptive Mesh Refinement method a coarse grid is advanced (in time) first and then all the subgrids are integrated to the same time level. Boundary values are often computed by interpolation from the coarse grid (Berger & Olinger 1984). By contrast, we do not evolve a coarse grid and hence we cannot interpolate variables at the intermediate boundaries. Instead, we evolve the various

subgrids (zones) in order of increasing timesteps (i.e. in the sequence $k = 1, k = 2, \dots, k = N$). In this way, all of the subgrids, apart from the last one ($k = N$), need values of same variables, extrapolated from earlier times, at the outer subgrid boundary. On the other hand, boundary values at each subgrid inner boundary can be computed by interpolation in time from values previously calculated in the adjacent subgrid. Linear extrapolation and interpolation in time has been used.

4.2. Subgrid evolutionary algorithm

The subgrid evolutionary algorithm establishes the order and the conditions under which the various subgrids have to be advanced in time. The main criterion is to evolve the subgrids in order of increasing timestep. Initially, the solution is evolved for a given number of cycles n_g over all of the grid with the smallest timestep. When $n > n_g$, the subgrid evolutionary algorithm is activated. The evolutionary time $t_k^{n_k}$ and the timestep $\Delta t_k^{n_k+1/2}$ of all the subgrids are stored in a vector that is periodically updated. The choice of the subgrid evolved at each cycle and its timestep are decided according to the following steps: [1] The evolution always starts from the innermost ($k = 1$) subgrid, so that $t_1^{n_1} \geq t_2^{n_2}$. The innermost subgrid is always evolved according to the Courant timestep, which takes its minimum value in this zone. [2] The innermost subgrid is advanced in time until the difference between its coordinate time and the one of the neighboring subgrid does not exceed a given threshold:

$$t_1^{n_1} - t_2^{n_2} < \frac{\Delta t_2^{n_2+1/2}}{\delta} \quad (31)$$

where $\delta \geq 1$ is a fixed number. Inequality (31) tells the code if the difference in the evolutionary times between subgrid $k = 1$ and $k = 2$ is less than δ^{-1} times the timestep of subgrid $k = 2$. [3] If the difference between the coordinate times exceeds the threshold, subgrid $k = 2$ is advanced to the time level of the first subgrid so that $t_2^{n_2} = t_1^{n_1}$. At this point the time centered quantities of subgrids $k = 1$ and $k = 2$ are synchronized (but not the time shifted). [4] Then, the code checks whether the inequality corresponding to (31) for subgrids $k = 2$ and $k = 3$ is satisfied: $t_2^{n_2} - t_3^{n_3} < \Delta t_3^{n_3+1/2}/\delta$. If the separation in time is below the threshold, the evolution continues from the first subgrid. [5] If it is not, subgrid $k = 3$ is advanced up to the time level of subgrid $k = 2$ (which, at this stage, is also equal to $t_1^{n_1}$). Time centered variables are then synchronized (whereas time shifted quantities are not evaluated at the same time level). This procedure is repeated for all the subgrids. Note that the factor δ has a very important role. The smaller δ is the faster the code will evolve, since the k -th subgrid will be advanced fewer times with respect to the $(k - 1)$ -th subgrid. However, too small a value of δ may cause accuracy and stability problems because of the extrapolation of the variables at the outer subgrid boundary. By experimenting, we found that the value $\delta \simeq 5$ turns out to be a good compromise between computational speed and accuracy.

4.3. Synchronization at regridding

The innermost subgrid is regridded whenever the inner boundary of the innermost mass shell $r_{j_{min}}$ crosses radius r_{in} . Synchronization at regridding represents a major problem since not all variables on the grid are time-centered. We solve the problem in the following way. Suppose that we are in the need of performing a regridding and let \bar{N} be the number of grids which are advanced up to the same time level (see previous subsection). All the time-centered quantities of the subgrids interior to (and including) \bar{N} will be synchronized. As described in Section 3, we need to interpolate in radius all the variables (time-shifted

and time-centered). This means that also the time-shifted variables have to be synchronized. This is accomplished evolving all the $k \leq \bar{N}$ subgrids together for two cycles, i.e. forcing the timestep of all the subgrids to be equal to the Courant timestep of the innermost region. In this way, both time centered and time shifted quantities in all the subgrids with $k \leq \bar{N}$ are synchronized and a regridding of all of the variables can be performed. If $\bar{N} = N$, all the mesh is regridded.

4.4. Performance

We have tested the MTP procedure in different situations and using the test problems which will be described in the next sections. We have varied different parameters (δ , N , j_{max} , the number of points of each subgrid, etc.) and the procedure turns out to be stable and accurate. The gain in computational time for a run with a grid of 200 zones in a domain spanning 4 decades in radius is about a factor 7–8 using 4–5 subgrids. We found that, beyond a certain number of subgrids (which depends on the specific problem and integration domain), the gain in computational time depends mainly on the number of points and the position of the boundary of each subgrid and not very much on N . A typical run including hydrogen opacity and recombination takes about 10 days on a Digital ALPHA station 200 4/233.

The main limit of the MTP procedure is certainly related with the extrapolation to get boundary values at the subgrid boundaries. This may cause problems following the evolution of shocks or any type of sharp feature possibly present in the solution. Problems may also originate if the flow enters a regime in which there are very delicate balances of forces, as for example when the luminosity is very close to the Eddington limit (within 1%). In such cases, it is necessary to restore the one timestep integration for the time necessary to follow the development of sharp features or the evolution of sensitive regimes. However, if the prominent feature is not crossing the boundary between two subgrids or if the delicate regime is contained within one subgrid, the evolution can proceed reliably using the MTP procedure.

5. Initial conditions and relevant timescales

In a supernova explosion, fallback of material may occur when a reverse shock forms at the interface between the mantle and the hydrogen envelope of the progenitor star (see e.g. Woosley & Weaver 1995). After the shock has propagated toward the center, the mantle is set into homologous expansion and matter bound to the central remnant is accreted. A complete analysis of the fallback process should comprise the simultaneous study of the expanding hydrogen envelope and of the mantle, a region where large composition gradients develop. Due to the complexity of the process here we explore a simplified model that follows the radiative and dynamical evolution of an expanding “cloud” of fixed composition. All of the emitted energy comes from the release of heat residing in the gas originally or is generated by compressional heating in the course of accretion onto the black hole. Radioactive energy sources have not been included in our calculations. Thus, our model will not give an accurate representation of the light curve of a supernova which is provided, at and after the peak, by radioactivity. Our main purpose is simply to calculate the contribution coming from accretion onto the central black hole and give quantitative estimates of its importance.

At the onset of evolution the cloud has homogeneous density ρ_0 and is set into homologous expansion with a velocity profile $u = r/t_0$, where t_0 denotes the expansion time scale. The maximum velocity of the ejecta is $V_0 = u(r_{out}) = r_{out}/t_0$, where r_{out} is the outer radial boundary of the expanding cloud. The

temperature profile is taken to be equal to the “radiative zero solution” of Arnett (1980)

$$T(r, 0) = T_0 \left[\frac{\sin(\pi x)}{\pi x} \right]^{1/4}, \quad (32)$$

where T_0 is the initial temperature at the inner boundary and $x = r/r_{out}$.

Four parameters specify uniquely the dynamical and thermal state of the cloud, for a fixed composition: the total mass M_{cloud} , the radius r_{out} , the sound speed at the inner boundary $c_{s,0}$, and the ratio \bar{k} of the accretion timescale $t_{a,0}$ (defined below) to the expansion time t_0 . Five relevant timescales are involved in this phenomenon. Using the electron scattering opacity (for completely ionized hydrogen) as reference value, $k_{es} = 0.4 \text{ cm}^2 \text{ g}^{-1}$, they are defined as follows:

$$t_{a,0} = \frac{GM_{bh}}{c_{s,0}^3} \quad (33)$$

$$t_0 = \frac{r_{out}}{V_0} \quad (34)$$

$$t_{diff} = \left[\frac{1}{4\pi} \frac{k_{es}}{c} M_{cloud} \right]^{1/2} \frac{1}{V_0^{1/2}} \quad (35)$$

$$t_{trans} = \left[\frac{3}{4\pi} k_{es} M_{cloud} \right]^{1/2} \frac{1}{V_0} \quad (36)$$

$$t_{rec} = t_0 \frac{T_0}{T_{rec}}. \quad (37)$$

$t_{a,0}$ and t_0 are the initial accretion and expansion timescales. The diffusion timescale, t_{diff} , represents the time for the radiation to diffuse out of an homogeneous expanding cloud. It can be estimated considering $t_{diff} \sim \tau_{es}(t_{diff})r_{out}(t_{diff})/3c$, where $3c/\tau_{es}(t_{diff})$ is the photon diffusion velocity and τ_{es} is the electron scattering optical depth. The timescale t_{trans} represents the time at which the cloud becomes transparent because of the decrease in density caused by the expansion; it is the time at which the photon mean free path $\lambda(t_{trans}) = 1/k_{es}\rho(t_{trans})$ is of the order of the cloud radius $r_{out}(t_{trans})$. For free expansion, the density decreases as $\rho \propto t^{-3}$. The recombination timescale t_{rec} is estimated calculating the time at which the gas temperature drops below the recombination temperature T_{rec} , as a consequence of adiabatic expansion; for a $\Gamma = 4/3$ polytrope, $T \propto \rho^{1/3} \propto t^{-1}$.

We consider a series of models selected on the basis of a predetermined hierarchy of timescales which will guide our understanding (for the parameters and related timescales see Table 1). Models 0, I, II and III deal with a cloud of fully ionized hydrogen for which the recombination time $t_{rec} \rightarrow \infty$. Models IVa and IVb allow for recombination: they have $T_{rec} \simeq 10^4 K$ and $t_{rec} \leq t_{diff}$. In all models, the mass of the central black hole is taken to be $M_{bh} = 1.5M_{\odot}$.

The first set of models (0 and I) have been introduced mainly to test our general relativistic radiation hydrodynamic code against previous numerical and analytical results. The choice of the parameters for the other models follows from the requirement that the hierarchy of relevant timescales reflects that for a realistic supernova model. For example, for the inferred parameters of the hydrogen envelope of SN1987A, we have: $t_{a,0} \ll t_0 \ll t_{rec} < t_{diff} \ll t_{trans}$ (see Table 2). The second set of runs (models II and III) do not include recombination and for them $t_{a,0} \ll t_0 \ll t_{diff} \ll t_{trans} \ll t_{rec}$. In practice, in these models, the photons have time to diffuse outwards before recombination takes place. Although they do not reflect the

true physics, these models are important to understand the role played by the central accreting black hole in shaping the light curve (in particular at late time). Since they have mainly a “pedagogical” purpose, we decided to run these models with a relatively small cloud mass ($M_{cloud} = 10^{-2}M_{\odot}$) and in turn small accreted mass. In this way t_{diff} and t_{trans} are decreased and, consequently, the computational time is significantly reduced. Note that, because t_{diff} and t_{trans} have the same dependence on the cloud mass, decreasing M_{cloud} does not alter the hierarchy of timescales as long as $t_0 < t_{diff}$. It should be noted also that in varying \tilde{k} (i.e. the expansion velocity V_0) the hierarchy of “radiative timescales” remains unchanged. In fact, from equations (35) and (36)

$$\frac{t_{diff}}{t_{trans}} = \frac{1}{\sqrt{3}} \left(\frac{V_0}{c} \right)^{1/2}. \quad (38)$$

In examining models I, II and III, we will assume that the opacities are given by

$$k_P = 10^{-2}k_{es} \left[1 + 10^2 e^{-(r/3r_{jmin+1})^2} \right], \quad (39)$$

$$k_R = k_{es} = 0.4 \quad \text{cm}^2 \text{ g}^{-1}. \quad (40)$$

The expression for k_0 has a maximum at $r = r_{jmin}$ and then goes rapidly to a constant value of $10^{-2}k_{es}$. This expression has been used for convenience to keep the inner core in LTE as long as possible in order to avoid the decrease in time-step caused by the inward motion of the inner boundary.

The last set of runs (models IVa and IVb) is a step forward to the study of more realistic models with $t_{a,0} \ll t_0 \ll t_{rec} < t_{diff} \ll t_{trans}$. Table 2 contains the relevant parameters for SN1987A describing the post-shock structure of hydrogen envelope and mantle (after the reverse shock has reached the center) as deduced from Arnett (1996) and Chevalier (1989), respectively. As can be seen by comparing Tables 1 and 2, model IVb has quite realistic initial parameters, although they do not match exactly the ones characterizing the hydrogen envelope in SN1987A. The calculation of a SN1987A-like model would be at least 5–6 times longer computationally. Because of the preliminary nature of the present investigation, we have not attempted such a calculation.

6. Numerical results

In this section we present results of the numerical calculation of the dynamical and thermal structure of the expanding cloud, starting from the initial conditions outlined in the previous section. All the light curves presented in the figures have been computed using w_1 calculated at the last grid point μ_{jmax} (which corresponds to the outermost radius r_{out}). It is

$$L(r_{out}) = 4\pi r_{out}^2 w_1(r_{out})c. \quad (41)$$

In equation (41), $L(r_{out})$ is the luminosity measured in the comoving frame. To obtain the luminosity seen by a distant Eulerian observer L_{∞} , one must transform to the Eulerian frame. However, at the outer boundary r_{out} , general relativistic effects can be neglected and the flow velocity V_0 never exceeds $0.1c$. Then, to calculate L_{∞} we can safely ignore relativistic corrections and write

$$L_{\infty} = L(r_{out}). \quad (42)$$

In the following we will always refer to the luminosity and accretion rate in units of the corresponding Eddington values for Thomson scattering in a completely ionized hydrogen gas. It is

$$l = \frac{L}{L_{Edd}} \quad (43)$$

$$\dot{m} = \frac{\dot{M}_0}{\dot{M}_{Edd}} \quad (44)$$

where $L_{Edd} = 4\pi GM_{bh}c/k_{es} = 1.3 \times 10^{38}(M_{bh}/M_\odot)$ erg s⁻¹, $\dot{M}_{Edd} = L_{Edd}/c^2 = 2.3 \times 10^{-9}(M_{bh}/M_\odot)M_\odot$ yr⁻¹ and the local accretion rate \dot{M}_0 has been defined by

$$\dot{M}_0 = 4\pi r^2 \rho u c. \quad (45)$$

6.1. Model 0: polytropic accretion – comparison with CSW

These models have been run to test the code and to compare our numerical results with those obtained by CSW. Two set of calculations were performed: accretion of a polytropic $\Gamma = 4/3$ gas with no radiation (see also Zampieri 1997) and accretion of a radiation dominated, completely ionized hydrogen gas with constant opacity. In the first set of runs, we considered two models with $\tilde{k} = 0.01$ and $\tilde{k} = 1$ and with the same value of the initial sound velocity ($c_{s,0} = 10^8$ cm s⁻¹). The agreement with the results of CSW is good: the density profile and the accretion rate as a function of time differ at most by $\sim 5\%$ percent. As already mentioned, we have tested these models changing a number of parameters such as the number of points, the position of the inner boundary, the number of subgrids, the position of the subgrid boundaries and δ . We found that the numerical results agree to within a few percent. The second set of runs includes radiation. The initial parameters are the same of the polytropic models. The absorption opacity was taken to be sufficiently high that, during dynamical evolution, matter and radiation were always in LTE over most of the integration domain. Furthermore, the evolutionary time is smaller than the diffusion timescale, so that the evolution is quasi adiabatic. In these conditions we expect that the solution should agree with the one obtained in the adiabatic case. The comparison of the accretion rate versus time with the results for a $\Gamma = 4/3$ polytrope shows agreement at the 1–2% level. We have also tested that, rescaling the flux mean opacity, the flow dynamics remains unchanged. This is the expected behavior for a radiation dominated optically thick gas, since the radiative force $k_1 w_1 \propto (1/3b\rho)(w_0)_{,\mu}$ and the radiation energy density gradient is basically insensitive to an overall rescaling of k_1 .

6.2. Model I: comparison with Arnett’s analytic solution

If the initial accretion timescale $t_{a,0}$ is longer than the diffusion timescale t_{diff} , the thermal and radiative structure of the envelope resembles that of a hot cloud that is cooling because of expansion and of emission of radiation. Figure 1 shows the light curve for model I for which $t_{a,0} \sim t_{diff}$. The filled squares are the computed points and the solid line gives the analytic solution for a pure radiation pressure, constant density (and opacity) gas given by Arnett (1980; “radiative zero solution”)

$$l = l_0 e^{-[t/t_{diff,0} + t^2/(\alpha_l t_{diff}^2)]}, \quad (46)$$

where $t_{diff,0} = 3k_{es}\rho_0 r_{out}^2/\pi^2 c$, $\alpha_l = 18/\pi^2$ and l_0 is the luminosity scale

$$l_0 \simeq \frac{2}{3} \frac{r_{out}}{r_s} \frac{aT_0^4}{\rho_0 c^2}. \quad (47)$$

In equation (47) r_s is the Schwarzschild radius. Since $t_{diff,0} \gg t_{diff}$, at late times the surface luminosity falls as a gaussian. As can be seen from the figure, the agreement between the numerical and analytical results is excellent. For $t < t_{diff}$ the luminosity is constant because the decrease in the radiation energy density gradient is exactly compensated by the increase in both the photon mean free path and the photospheric radius. When t becomes larger than t_{diff} , the internal energy is being exhausted and the luminosity falls off as a gaussian.

6.3. Model II: photon diffusion in a high temperature, expanding cloud with a central black hole

For the typical parameters of a supernova with a black hole mass of $\sim 1.5M_\odot$, the accretion timescale is usually much smaller than the diffusion timescale. The presence of the central black hole is “felt” by the expanding cloud. We have computed a model with $M_{cloud} = 10^{-2}M_\odot$, corresponding to $t_{diff}/t_{a,0} \simeq 5$. The results are shown in Figures 2–4. In Figure 2, for $t < t_{diff}$ the luminosity is roughly constant and is still due to the emission of the cloud internal energy. The differences with respect to the analytic solution (equation [46]) can be explained in terms of the different hierarchy of timescales ($t_{a,0} < t_{diff}$) and of the increasing importance of the gas pressure. In fact, for this model the initial value of the radiation to gas pressure ratio is not very large (in particular near to the outer boundary where the temperature drops rapidly). Then, equation (46) is no longer a good approximation to the numerical solution. At $t \simeq t_{diff}$, the initial exponential decline in the light curve turns into a steep power law. *This is the first signature of the presence of the central black hole.* In fact, if no black hole were present, one would expect the light curve to fall off as a gaussian with time. The radiative energy emerging at this stage has been produced by accretion during the early phases of the evolution and transported outward diffusively. At $r_0 = 0.3r_{a,0}$ the maximum value of the diffusive accretion luminosity $l \simeq 0.5$ is reached at $t \simeq t_{a,0}$ (see Figure 3a) slightly after the peak in the accretion rate (Figure 3b). After traveling outwards through the opaque cloud, this accretion energy emerges on a diffusion timescale: this corresponds to the point, along the light curve, at which the analytic calculation fails to reproduce the actual behavior. Later, the cloud becomes transparent ($t \sim t_{trans}$), and the central accreting black hole “becomes visible”. The steep decline of the light curve ceases and the emergent luminosity is entirely produced by accretion of the gravitationally bound gas. The internal accreting region is still optically thick. We note that, at times before t_{diff} , the heat content of the gas is dominated by radiation, but at times after t_{diff} it becomes dominated by the electrons, protons and hydrogen atoms. At this stage, the timestep of the numerical integration becomes exceedingly small because the inner boundary has to be moved inward to recover the region where the radiation field is in LTE. In practice, this prevents us from studying numerically the very late–time evolution of the model. However, as we shall see later, the light curve can be equally well computed using a sequence of stationary models with progressively decreasing density at infinity (see next section).

Figure 4 summarizes the properties of the flow at different times along dynamical evolution. As shown in Figure 4a, at the onset of expansion the gas is outflowing with $u \propto r$. Very soon the inner low velocity shells start to accrete and free fall ($u \propto r^{-1/2}$) is rapidly achieved. Because the dynamical timescale in the inner part of the flow is much smaller than that in the outer envelope, in the inner accreting region the density profile adjusts very quickly to the $\rho \propto r^{-3/2}$ behavior (Figure 4b), as in stationary flows. In the outermost regions ρ remains nearly independent of radius and decreases with time ($\sim t^{-3}$) because of expansion (CSW). The evolution of the gas temperature is closely coupled with the properties of the radiation field (Figures 4c and 4d). In the inner accreting region, the temperature increases inward

($T \propto r^{-5/8}$; see e.g. Blondin 1986 equation [17]) because of the compressional work done by gravitational forces. In the outer expanding region, at early times T remains roughly constant with radius, except close to the outer boundary, where it drops significantly to transport photons outwards diffusively. In this respect, the temperature profile reflects the behavior of the solution of Arnett (1980). As shown in Figure 4c, during early evolution when gas and radiation are in LTE and $t < t_{diff}$, T drops adiabatically with time ($T \propto t^{-1}$), as expected for a freely expanding radiation dominated gas. In Figure 4d, we have plotted the luminosity profile at different times along dynamical evolution. At $t \sim 3t_{a,0}$, l has two maxima: the first represents the accretion luminosity produced by the central black hole, whereas the second is due to the emission of the internal energy stored in the cloud. After the initial transient phase, the accretion luminosity decreases steadily with time. The diffusive luminosity of the cloud stays almost constant up to $t \sim t_{diff}$ and then falls off as a gaussian. At $t \sim 500t_{a,0}$ the cloud becomes transparent to the central accreting region (see the curve at $t = 1034t_{a,0}$ in Figure 4d).

6.4. Model III: photon diffusion in a high temperature, slowly expanding cloud with a central black hole

As we already noted, the hierarchy of “radiative” timescales remains unchanged as we vary the velocity of the ejecta V_0 . So the light curve of model III (same parameters of model II but $\tilde{k} = 0.1$; see Table 1) shows the same basic features of model II: initial plateau due to the emission of internal energy, a steep exponential decline turning into a power law at $t \sim t_{diff}$ because of the emergence of the initial transient accretion energy, cessation of the rapid decline due to the clearing of the cloud, revealing the presence of the central black hole (see Figure 5). However, some differences can be noted. First, comparing Figure 5 with Figure 2, it appears that the power law decline after $t = t_{diff}$ has a different slope. This can be explained in terms of the different expansion timescale. Since model III has an outward expansion velocity 10 times smaller than model II, less work is being done by the gas and the internal energy suffers less adiabatic degradation. Also the energy released by accretion undergoes less degradation and can then produce a flatter tail in the light curve after $t \sim t_{diff}$. Second, because of the lower expansion velocity of model III, for a certain time the outer part of the expanding cloud remains opaque whereas the central part is optically thin. During this phase, the accretion luminosity produced in the inner region is partly absorbed by the outer optically thick region. This is the reason for the decrease in luminosity close to the outer boundary at $t \simeq 2400t_{a,0}$ in Figure 6.

6.5. Model IV: clearing from expansion and recombination

As illustrated in Figure 4c, by the time that the cloud becomes optically thin because of expansion the temperature has already dropped well below $10^4 K$, the temperature at which hydrogen recombines. In fact, in a realistic model of a supernova explosion, the clearing of the hydrogen envelope takes place because of recombination. For this reason we consider a pure hydrogen gas with variable degree of ionization in model IVa and IVb. The ionization coefficient is computed from the Saha equation. As can be seen looking at the temperature and luminosity profiles of model IVa (Figures 8a and 8b), for $t < t_{rec}$ the evolution is very similar to that of model II. At $t \sim t_{rec}$ hydrogen starts to recombine. The recombination process is very fast and generates a recombination wave that propagates rapidly through the envelope (Figure 8a). Outside the recombination front the gas is optically thin, whereas inside the mean free path is so small that the gas is everywhere opaque. The recombination front almost coincides with the photosphere. Note the

sudden rise in luminosity in Figure 8b after the recombination front has propagated inward. As noted by Woosley (1988), during this phase, the radiation does not have time to diffuse through the photosphere; the photosphere instead moves to the radiation, releasing all of the internal energy. The huge amount of internal energy released gives rise to a big bump in the light curve at $t \sim t_{rec}$ (see Figures 7 and 9a). After the maximum, the luminosity falls off abruptly (see also Figure 8b). In contrast to models II and III, no power law decay can be observed after maximum. The reason is that the fast inward motion of the recombination front has liberated all of the internal energy before it could diffuse outwards. Also the initial transient accretion energy, stored as internal energy in the gas flow, has been completely liberated and contributes to the big recombination bump in the light curve. During this phase our computed light curves are similar to those calculated by Woosley (1988) for stars with low envelope mass. In this respect they resemble the light curve of a Type II–Type Ib supernova. At late times, after that the recombination front has propagated down to the inner accreting region, the light curve is entirely powered by accretion onto the central black hole and the luminosity decreases as a power law with time (see next section). In model IVb, the total mass accreted onto the central black hole is $\sim 2 \times 10^{-5} M_{\odot}$.

In Figure 8c we follow the evolution of the recombination front as a function of time (for model IVa). The front clearly stalls as soon as it approaches the innermost region where compressional heating due to accretion overcomes radiative cooling. The density and velocity profiles are largely unaffected by the propagation of the recombination front, which instead influences the light curve and thermal state of the cloud. In Figures 9b we plot the effective temperature, T_{eff} , and the gas temperature at the photospheric radius, T_{ph} , as a function of time for model IVb:

$$T_{eff} = \frac{L(r_{ph})}{4\pi r_{ph}^2 \sigma} \quad T_{ph} = T(r_{ph}), \quad (48)$$

where r_{ph} is the photospheric radius (i.e. the radius at which the effective optical depth is equal to unity). As can be seen from Figure 9b, during the phase of “adiabatic” expansion, the effective temperature decreases with time to $\sim 4000K$. When recombination takes place, the photosphere starts to recede through the envelope and T_{eff} rises to $\sim 10^4K$. From this moment on the photosphere is located in the inner accreting region where the compressional heating is balanced by radiative recombination. Furthermore, for $t > 10^3 t_{a,0}$ the gas photospheric temperature stays very close to the effective temperature, which suggests that the emitted continuum spectrum should be roughly a blackbody. When all of the outer hydrogen envelope is recombined and all of its internal energy has been emitted, the fall in luminosity ceases and the light curve starts to be dominated by the accretion luminosity of the gravitationally bound shells. At this point the timestep of the numerical integration becomes very small. However, as we will discuss in the next section, the asymptotic curve $l = l(\dot{m})$ can be estimated using a sequence of stationary models with progressively decreasing density at infinity.

Consider the early behavior of model IVb (see Figures 10), which has the largest initial cloud mass M_{cloud} . The large amount of mass that falls back within the first few hours gives rise to an initial (diffusion) luminosity transient that reaches the Eddington limit (see Figure 10b). At this point the flow starts to be “self-regulated”. As the accretion rate increases, it drives the luminosity above the Eddington limit. Then, the radiative force eventually pushes outwards the accreting gas (note the sign inversion of the velocity of the intermediate shells at $t \simeq 2t_{a,0}$ in Figure 10a). The flow readjusts itself in such a way to maintain the luminosity close to the Eddington limit. This delicate balance between radiative and gravitational forces governs the flow dynamics and allows the gas to radiate very close to the Eddington limit during the first evolutionary phase. This result is in agreement with the findings of CSW. In their $\Gamma = 4/3$ polytropic calculation, they have shown that in flows with $\tilde{k} \ll 1$ the pressure pushes initially bound shells

outwards, preventing them from accreting. Since an optically thick, radiation dominated flow is dynamically equivalent to a $\Gamma = 4/3$ polytrope, the gas pressure gradient in the CSW models acts much in the same way as the radiative force in our models.

7. Late-time light curve

CSW showed that in polytropic flows with $\tilde{k} = t_{a,0}/t_0 > 1$, pressure forces act as a small perturbation and the accreting gas behaves as a nearly collisionless fluid. In this case the total mass accreted is (CSW, equation [17])

$$M_{dust} \simeq \frac{8\pi}{3} GM_{bh} \rho_0 t_0^2, \quad (49)$$

and the late-time evolution of the accretion rate (in units of the Eddington rate) is equal to (CSW, equation [29])

$$\dot{m}(t) \simeq \frac{4\pi^{2/3}}{9} \rho_0 t_0 c k_{es} \left(\frac{t}{t_0} \right)^{-5/3}. \quad (50)$$

In the opposite regime, $\tilde{k} = t_{a,0}/t_0 < 1$, pressure forces significantly affect the motion. After a time $t \sim 10t_{a,0}$ the flow evolves along a sequence of quasi-stationary, Bondi-like states, with a time dependent \dot{m} determined by the slowly varying density at large distances (CSW, equation [45])

$$\dot{m}(t) \simeq \lambda_\Gamma GM_{bh} c k_{es} \frac{\rho_\infty}{c_{s,\infty}^3}, \quad (51)$$

where $c_{s,\infty} = (\Gamma K \rho_\infty^{\Gamma-1})^{1/2}$ is the sound speed (K and Γ are the polytropic constant and the polytropic index) and $\lambda_\Gamma = 0.25[2/(5-3\Gamma)]^{(5-3\Gamma)/2(\Gamma-1)}$. For homologous expansion $\rho_\infty = \rho_0(1 + \tilde{k}t/t_{a,0})^{-3}$. The persistence of a Bondi-like behavior is however limited to an interval of time between $10t_{a,0} < t < t_{tr}$. At late times $t > t_{tr}$, the flow enters the dust regime and the accretion rate falls like $\dot{m} \propto t^{-5/3}$. The transition time t_{tr} is estimated to be $\sim 9\tilde{k}^{-3}t_{a,0}/2$, for $\Gamma = 4/3$, and is the time when the instantaneous Bondi accretion radius reaches a position where the fluid is unbound and flying away supersonically. For a flow with $\tilde{k} < 1$, the mass that has fallen back can be estimated multiplying the Bondi accretion rate $\dot{M}_{Bondi} = 4\pi\lambda_\Gamma\rho_0 r_{a,0}^3/t_{a,0}$ by the accretion timescale $t_{a,0}$, which gives

$$M_{Bondi} \simeq 4\pi\lambda_\Gamma\rho_0 \frac{[GM_{bh}]^3}{c_{s,0}^6}. \quad (52)$$

As can be seen from the previous equation, the total accreted mass is very sensitive to the actual value of $c_{s,0}$. M_{Bondi} is only a tiny fraction $3\lambda_\Gamma\tilde{k}^2/2 \sim t_{a,0}^2/t_0^2$ of the mass accreted if the flow was collisionless (see equation [49]). In fact, for fixed ρ_0 and t_0 , the most favorable situation (when the accreted mass is maximum) occurs if the sound velocity is so low that pressure forces can be neglected, i.e. if the flow is collisionless. In this regime, t_0 becomes the relevant timescale for accretion and the total accreted mass is $\sim M_{dust}$.

Models IVa and IVb have $\tilde{k} = 1$ and $\tilde{k} = 0.1$ respectively. In IVa, the fluid is nearly collisionless and, after time $t \simeq 10t_{a,0}$, we find that \dot{m} (plotted in Figure 11) is well approximated by equation (50). In IVb, the expansion timescale is instead larger than the accretion time and, at intermediate times ($t_{a,0} < t < 4.5 \times 10^3 t_{a,0}$), the flow is expected to evolve along a sequence of quasi-steady states characterized by $\Gamma = 4/3$ and $\dot{m} \propto t^{-3/2}$ (equation [51]). As shown in Figure 11, the accretion rate decays approximately as $t^{-3/2}$, as long as $t \lesssim 300t_{a,0}$. We then observe a slight bending toward higher rates. Later on, the

accretion rate changes slope again and \dot{m} starts decaying as $t^{-5/3}$: thereafter, the flow behaves as dust. Note that, due to the small envelope mass (for IVa) and small \tilde{k} (for IVb), the total mass accreted is tiny in these two models.

In Figure 12 we have plotted \dot{m} as a function of radius at $t = 6 \times 10^3 t_{a,0}$ for model IVb. As can be seen, in the inner region the accretion rate is nearly independent of radius. This means that the evolution follows a sequence of quasi-stationary states. Indeed, the inner part of the accretion flow, where most of the luminosity is produced, shows the same density and temperature structure of the stationary models of spherical accretion onto black holes computed by Blondin (1986), Park (1990) and Nobili, Turolla & Zampieri (1991). Therefore, we can extrapolate the late-time evolution of the luminosity using their results. As shown in Figure 13, the path described along the luminosity–accretion rate plane is in fair agreement with the solid line, which represents the analytic expression of $l = l(\dot{m})$ for stationary models derived by Blondin (1986)

$$l \simeq 3 \times 10^{-7} \left(\frac{M_{bh}}{M_{\odot}} \right)^{-1/3} \dot{m}^{5/6} \quad \dot{m} \geq 10. \quad (53)$$

Equation (53) is obtained assuming that all of the compressional work done by the gravitational field is converted into radiation in the inner accreting region where $T \propto r^{-5/8}$ (Blondin 1986). For $\dot{m} \geq 10$, Blondin’s approximation provides a satisfactory fit to the numerical value of $l = l(\dot{m})$ calculated by Nobili, Turolla & Zampieri (1991). In Figure 14 we plot the light curves of model IVa and IVb computed numerically along with their asymptotic behavior. For model IVa, the late-time accretion rate is estimated using equation (50). For model IVb, the late time \dot{m} is approximately calculated from $\dot{m}(t) = \dot{m}(t_{ref})(t/t_{ref})^{-5/3}$, where $t_{ref} = 6.5 \times 10^3 t_{a,0}$ and $\dot{m}(t_{ref}) = 8.1 \times 10^3$ are taken from the computed model. Figure 14 shows that the analytic extrapolation is in fair agreement with the points computed numerically.

In the interval $0.03 \lesssim \dot{m} \lesssim 10$, Blondin’s approximation is only approximately correct and is invalid below ~ 0.03 , as the flow becomes transparent to its own radiation. To estimate the very late-time accretion luminosity one can adopt (as an order of magnitude estimate) the interpolation of the optically thin, stationary spherical accretion models (Park 1990; Nobili, Turolla, & Zampieri 1991) for which

$$l \propto \dot{m}^2 \quad \dot{m} \lesssim 0.03. \quad (54)$$

In light of these findings, we can derive a simple scaling relation for the luminosity emitted by the black hole soon after the recombination front has propagated down to the inner accreting region. The scaling involves the main physical parameters of the flow at the onset of evolution. If the fluid is collisionless (hypothesis appropriate for model IVa) we can estimate the accretion rate according to equation (50)

$$\dot{m}(t_{rec}) \simeq \frac{4\pi^{2/3}}{9} \rho_0 t_0 c k_{es} \left(\frac{t_{rec}}{t_0} \right)^{-5/3}. \quad (55)$$

Adopting equation (53) as scaling relation between l and \dot{m} , we find a luminosity at t_{rec}

$$L_{rec} \sim 1.2 \times 10^{40} (\rho_0 t_0)^{5/6} \left(\frac{t_{rec}}{t_0} \right)^{-25/18} \text{ erg s}^{-1}. \quad (56)$$

Using as reference values those of Table 1 and a value of $T_{rec} \sim 10^4 \text{K}$, for model IVa we estimate a luminosity $L_{rec} \sim 1.4 \times 10^{35} \text{erg s}^{-1}$ which is in close agreement with the numerical results. Equation (56) thus provides an approximate expression for the accretion luminosity soon after clearing by recombination. L_{rec} is a function of ρ_0 , T_0 and t_0 at the onset of the explosion. Subsequently, the luminosity will decline with time as $t^{-25/18}$ (from equations [50] and [53]).

If the flow is radiation pressure dominated (model IVb) we can instead estimate the accretion rate at $t \simeq t_{rec}$ from equation (51). Thus, we have

$$\dot{m}(t_{rec}) \simeq \lambda_{4/3} GM_{bh} c k_{es} \frac{\rho_0}{c_{s,0}^3} \left(\frac{t_{rec}}{t_0} \right)^{-3/2} \quad (57)$$

and the luminosity turns out to be

$$L_{rec} \sim 5.4 \times 10^{23} L_E \left(\frac{\rho_0}{c_{s,0}^3} \right)^{5/6} \left(\frac{t_{rec}}{t_0} \right)^{-5/4}. \quad (58)$$

For model IVb $L_{rec} \sim 10^{35} \text{erg s}^{-1}$. The above relation can be applied to our numerical models since the density evolution is seen to preserve a self-similar character, even during the propagation of the recombination front: inside the accretion region, $\rho(r, t) \simeq \rho_0 (t/t_0)^{-3} [r/r_a(t)]^{-3/2}$, where $r_a(t) \simeq r_{a,0} (t/t_0)$ denotes the current value of the accretion radius. Equation (58) fixes the “level” of the luminosity at the moment of clearing of the envelope. Its time evolution will then depend on the nature of the flow after t_{rec} . At late times we expect the transition to dust giving a luminosity $L \propto t^{-25/18}$ (as long as $\dot{m} \gtrsim 10$).

In the next section we will use this scaling to give a first estimate of the time at which the bolometric light curve of SN1987A becomes dominated by the accreting black hole.

8. Discussion and conclusions

The computed light curves of model IVa and IVb show that, prior to recombination, the release of internal energy from the expanding stellar envelope dominates over accretion. Although during the first few hours the diffusive accretion luminosity can be very close to the Eddington limit, the diffusive and advection luminosities of the hot outer layers are largely superEddington. As shown by model IVb, during recombination the computed light curve shows the typical behavior observed in Type II-Ib supernovae with low envelope mass. The luminosity at peak is comparable to that of SN1987A because the initial sound velocity of the hydrogen envelope is similar (see Tables 1 and 2). The high expansion velocity and low envelope mass of model IVb reduce all of the relevant timescales (see Table 1) so that recombination takes place at about 10 days after the onset of the explosion, instead of the 40–50 days inferred for SN1987A (see e.g. Woosley 1988). Nevertheless, our numerical results clearly indicate that no distinct signature in the light curve is found that could reveal the accreting black hole during this initial evolutionary phase. Only after the sharp decrease in luminosity due the clearing of the envelope by recombination, the accreting black hole starts to power the bolometric light curve of the computed models and l decreases as $t^{-25/18}$ (see equations [50] and [53]).

Slightly after maximum, SN1987A was powered by the radioactive decay of ^{56}Co and ^{57}Co and, at present, its light curve is consistent with emission from the decay of ^{44}Ti (Suntzeff 1997; see Figure 14). Can we discern the luminosity emitted by the accreting black hole above the contribution resulting from ^{44}Ti ? As already noted, the accretion history is very sensitive to the value of the sound speed (see equation [52]). Depending on the actual value of $c_{s,0}$ in the inner part of the ejecta surrounding the compact remnant (the mantle), the accretion rate and, in particular, the total accreted mass vary significantly. An upper limit to the accretion luminosity can be inferred taking the initial parameters of the mantle quoted by Chevalier (1989; see Table 2). In this case, $c_{s,0} \simeq 3 \times 10^7 \text{ cm s}^{-1}$ and $t_{a,0} \sim t_0$, giving substantial fallback. The mass accretion rate can be computed using equation (50) and the luminosity according to equation (53). Thus,

we have

$$l \simeq 3 \times 10^{-7} (\rho_0 t_0 c k_{es})^{5/6} \left(\frac{t}{t_0} \right)^{-25/18}. \quad (59)$$

Following Chevalier (1989), we adopt $\rho_0 t_0^3 \approx 10^9$ cgs and $t_0 \approx 7000$ seconds, yielding a maximum accretion luminosity

$$l \simeq \frac{8 \times 10^{-3}}{(M_{bh}/M_\odot)^{1/3} [t(\text{years})]^{25/18}}. \quad (60)$$

Equation (60) implies $L \simeq 5 \times 10^{34} \text{erg s}^{-1}$ after $t \approx 10$ years, which is well below the present day bolometric luminosity of the remnant ($\sim 10^{36} \text{erg s}^{-1}$; Suntzeff 1997) and also smaller than the luminosity estimated to result from radioactive decay. Thus, there is no observation that rules out the possibility that a black hole resides inside the SN1987A remnant. At very late times, when $\dot{m} \lesssim 0.03$, the corresponding upper bound would be

$$l \simeq 2 \times 10^{-8} (\rho_0 t_0 c k_{es})^2 \left(\frac{t}{t_0} \right)^{-10/3}, \quad (61)$$

or, using Table 2,

$$l = \frac{7 \times 10^{-8}}{[t(10^3 \text{years})]^{10/3}}. \quad (62)$$

In Figure 14 we plot the late-time light curve of SN1987A calculated using equations (60) and (62). As radioactive decay plummets at around 270–2700 years, it is clear that the black hole would only appear after about 900 years irrespective of the detailed numbers. After this time has elapsed, the luminosity of the remnant would be $\sim 10^{32} \text{erg s}^{-1}$, too dim to be detectable using present technology, and possibly even a challenge for our distant descendants, as it would be hard to distinguish from the multitude of low mass stars crowding its field in the Large Magellanic Cloud.

Since we have carried out a frequency-integrated calculation, we can only estimate the emission properties from the effective temperature and the photospheric gas temperature. During the optically thick accretion phase (when $\dot{m} > 0.03$), the numerical results show that T_{eff} and T_{ph} are very close and have a value $\sim 8000\text{--}10000$ K. This corresponds to a mean photon energy in the few eV range, for which the bulk of the emission is expected in the visible band. Since T_{eff} and T_{ph} are close together the continuum spectrum should be roughly a blackbody. This is not surprising because the emission processes are thermal and the gas in the inner accreting region is optically thick. Only at very late times ($t \gtrsim 2500$ yr), the accretion flow becomes optically thin and the gas temperature reaches very high values ($10^8\text{--}10^9$ K; this regime has not been treated in the present numerical computation). So, at the time of emergence, the inner part of the accretion flow will be still optically thick and will be emitting roughly a black body spectrum peaked in the visible band.

A number of interesting issues can be addressed within the framework presented in this paper. Can the presence of a stellar black hole in SN1987A be deduced from the excess accretion luminosity it produces? What is the observational signature of the explosion of more massive progenitors (those with $M \sim 30M_\odot$) on the light curve of the remnant? Woosley, & Timmes (1996) suggested that a distinguishing signature would be a bright plateau that steeply falls to very low or zero luminosity, similarly to what found in our models.

A number of assumptions limit the applicability of our results, amongst, the hypothesis of spherical symmetry and the simple chemical composition considered. As a result of an asymmetry in the explosion mechanism, black holes may come to birth with significant intrinsic velocities (a few $\times 100$ km s^{-1}). This is certainly observed for pulsars whose mean birth speed is around 250–300 km s^{-1} (Hansen & Phinney

1997; Cordes & Chernoff 1997). However, since the initial sound speed of the ejecta can be of the order of 10^3 km s^{-1} , the accretion will proceed essentially subsonically. The central compact remnant tends to comove with gas expanding at its velocity and, if the ambient density is uniform, the conditions are independent of position within the core, as in the cosmological Hubble flow. Thus, even a relatively large intrinsic velocity should not strongly modify the results presented here. Deviations from spherical symmetry can arise if infalling matter has even a small amount of specific angular momentum, which presents a barrier to spherical infall (Chevalier 1996). In the case of SN1987A, the fact that the observed neutrino burst is consistent with implosion models without rotation (Burrows 1988) seems to indicate that angular momentum of matter initially close to the black hole was not very important (see also Chevalier 1996). In this case, the accretion should have proceeded almost radially, although mixing of outer mantle material with significant angular momentum into the inner region could modify our picture.

A more realistic model with shell-like chemical composition and heating due to radioactive decay will enable us to address more quantitatively the problem of the visibility of black holes in otherwise successful supernova. This analysis will also set the basis for studying fallback onto a nascent neutron star in order to verify whether major outflows establish that reverse the process, during the decline of the supernova light curve.

This work was supported in part by NSF grants AST 93–15133, AST 96–18524 and NASA grants NAG–5–2925 and NAG–5–3420 at the University of Illinois at Urbana–Champaign and by NSF grant 93–15375 and NASA grant NAG–5–3097 at Cornell University. Monica Colpi would like to thank the Department of Physics of the University of Illinois at Urbana–Champaign for its hospitality during part of this work. Luca Zampieri would like to thank Luciano Rezzolla for carefully reading and suggesting improvements of Section 4.

A. Finite difference equations

The full set of finite difference equations of relativistic hydrodynamics plus the radiation moment equations are summarized in this appendix. The indexes j and n will be used to denote spatial and time dependence, respectively. As discussed in the main text, ρ , B , w_0 and a are evaluated at mid-zones ($j + 1/2$), while r , M , u and w_1 are evaluated at zone boundary (j). Mid-zone variables can be easily computed from zone boundary variables as: $A_{j-1/2} = (A_j + A_{j-1})/2$, where A is any variable. To compute zone boundary quantities from mid-zone quantities, it is necessary to take into account for the nonuniform spacing of the grid. Using linear interpolation, it is

$$A_j = (\alpha A_{j-1/2} + A_{j+1/2}) / (1 + \alpha), \tag{A1}$$

where α is the fractional increment in grid spacing between successive zones (see Section 3). As far as time centering is concerned, u and w_1 are evaluated at an intermediate time level ($n + 1/2$; time-shifted), while all the other variables are centered at the full time level (n). Linear interpolation/extrapolation in time has been used when necessary.

Initial values for all the variables are specified on the grid according to what discussed in Section 5. Before starting the evolution, the radial component of the flow velocity u and the radiative flux w_1 are advanced at time level $t^{1/2}$ solving equations (3) and (24) with a forward time integration scheme.

The code starts to evolve first equation (8). Solving for the Eulerian radius at the new time level, we

obtain ($j_{min} \leq i \leq j_{max}$)

$$r_j^{n+1} = r_j^n + \Delta t^{n+1/2} a_j^{n+1/2} u_j^{n+1/2}, \quad (\text{A2})$$

where $\Delta t^{n+1/2}$ is the timestep between level n and $n+1$ and $a_j^{n+1/2}$ is interpolated at the zone boundary in space and extrapolated at time level $n+1/2$. Then, the time evolution of the matter density is computed. Equation (4) can be formally integrated in time and solved for $\rho_{j-1/2}^{n+1}$ using the Crank–Nicholson operator (see e.g. May & White 1967; $j_{min} + 1 \leq j \leq j_{max}$)

$$\rho_{j-1/2}^{n+1} = \rho_{j-1/2}^n \frac{(r^2)_{j-1/2}^n}{(r^2)_{j-1/2}^{n+1}} \frac{1 - F_\rho/2}{1 + F_\rho/2}, \quad (\text{A3})$$

where

$$F_\rho = \Delta t^{n+1/2} a_{j-1/2}^{n+1/2} \left[\frac{u_j^{n+1/2} - u_{j-1}^{n+1/2}}{r_j^{n+1/2} - r_{j-1}^{n+1/2}} - 2\pi \frac{r_j^{n+1/2} (w_1)_j^{n+1/2} + r_{j-1}^{n+1/2} (w_1)_{j-1}^{n+1/2}}{\Gamma_{j-1/2}^{n+1/2}} \right]. \quad (\text{A4})$$

In equation (A3), $(r^2)_{j-1/2}^{n+1}$ has been computed in order to give the correct total volume of shell $j-1/2$ (May & White 1967). To derive equation (A3) and (A4), we used equation (5) and the two following relations, valid at constant Lagrangian time t :

$$r_{,\mu} = b\Gamma \quad (\text{A5})$$

$$\frac{\partial}{\partial \mu} = r_{,\mu} \frac{\partial}{\partial r}. \quad (\text{A6})$$

In equation (A4), $a_{j-1/2}^{n+1/2}$ and $\Gamma_{j-1/2}^{n+1/2}$ have been extrapolated at time level $n+1/2$.

After calculating the optical depth τ_j^{n+1} and the Eddington factor f_j^{n+1} with the advanced value of the matter density, the energy and the 0-th moment equations (equations [25] and [26]) are solved for $B_{j-1/2}^{n+1}$ and $(w_0)_{j-1/2}^{n+1}$ ($j_{min} + 1 \leq j \leq j_{max}$)

$$\begin{aligned} \frac{\epsilon_{j-1/2}^{n+1} - \epsilon_{j-1/2}^n}{\Delta t^{n+1/2}} + a_{j-1/2}^{n+1/2} (k_P)_{j-1/2}^{n+1/2} \left[B_{j-1/2}^{n+1/2} - (w_0)_{j-1/2}^{n+1/2} \right] + \\ + \frac{p_{j-1/2}^{n+1/2}}{\Delta t^{n+1/2}} \left(\frac{1}{\rho_{j-1/2}^{n+1}} - \frac{1}{\rho_{j-1/2}^n} \right) = 0 \end{aligned} \quad (\text{A7})$$

$$\begin{aligned} \frac{(w_0)_{j-1/2}^{n+1} - (w_0)_{j-1/2}^n}{\Delta t^{n+1/2}} - a_{j-1/2}^{n+1/2} (k_P)_{j-1/2}^{n+1/2} \rho_{j-1/2}^{n+1/2} \left[B_{j-1/2}^{n+1/2} - (w_0)_{j-1/2}^{n+1/2} \right] + \\ + (w_0)_{j-1/2}^{n+1/2} a_{j-1/2}^{n+1/2} \left[\left(\frac{4}{3} + f_{j-1/2}^{n+1/2} \right) \frac{1}{(r^2)_{j-1/2}^{n+1/2}} \times \right. \\ \left. \times \frac{u_j^{n+1/2} (r_j^{n+1/2})^2 - u_{j-1}^{n+1/2} (r_{j-1}^{n+1/2})^2}{r_j^{n+1/2} - r_{j-1}^{n+1/2}} - 3 \left(\frac{f u}{r} \right)_{j-1/2}^{n+1/2} \right] + \\ + \left(\frac{\Gamma}{ar^2} \right)_{j-1/2}^{n+1/2} \left[\frac{(w_1)_j (a_j)^2 (r_j)^2 - (w_1)_{j-1} (a_{j-1})^2 (r_{j-1})^2}{r_j - r_{j-1}} \right]^{n+1/2} - \\ - \left[\frac{4\pi r a}{\Gamma} \left(\frac{4}{3} + f \right) w_0 w_1 \right]_{j-1/2}^{n+1/2}, \end{aligned} \quad (\text{A8})$$

where $B_{j-1/2}^{n+1/2} = (B_{j-1/2}^n + B_{j-1/2}^{n+1})/2$ and $(w_0)_{j-1/2}^{n+1/2} = [(w_0)_{j-1/2}^n + (w_0)_{j-1/2}^{n+1}]/2$. Since ϵ , p and k_P are in general rather complicated functions of ρ and B (see e.g. equations [14], [15]), equations (A7) and (A8) form a highly non-linear system that has been solved by means of the Newton–Raphson method. To write the 0-th moment equation in finite difference form, $r_{,t}$ has been substituted with au (equation [8]) and the term $b_{,t}/b = -(\rho r^2)_{,t}/\rho r^2$ has been expressed using the continuity equation (4).

The time slice at constant t is a characteristic direction for equation (6) so that it can be formally integrated along the grid at the new time level t^{n+1} . Using the Leith–Hardy operator to approximate the exponential $\exp(-F_a) = \exp\{-\int[(e_{,\mu} - h\rho_{,\mu} - bs_1)/h\rho]d\mu\}$ in the interval $[\mu_{j-1/2}, \mu_{j+1/2}]$ (see May & White 1967), it reads ($j_{min} + 1 \leq j \leq j_{max}$)

$$a_{j-1/2}^{n+1} = \frac{(ah)_{j+1/2}^{n+1}}{h_{j-1/2}^{n+1}} \frac{1}{1 + F_a + F_a^2/2}, \quad (\text{A9})$$

where

$$F_a = \left\{ \frac{1}{(h\rho)_j} \left[\rho_j (\epsilon_{j+1/2} - \epsilon_{j-1/2}) - \frac{p_j}{\rho_j} (\rho_{j+1/2} - \rho_{j-1/2}) - \frac{\mu_{j+1/2} - \mu_{j-1/2}}{4\pi r_j^2 \rho_j} (s_1)_j \right] \right\}^{n+1}. \quad (\text{A10})$$

In equation (A10), ρ_j , p_j and $(h\rho)_j$ are linearly interpolated at the zone boundaries. The difference $\mu_{j+1/2} - \mu_{j-1/2}$ can be written as $(1 + \alpha)\Delta\mu_{j-1/2}/2$. Finally, the value of w_1 in s_1 has been linearly extrapolated at the new time level t^{n+1} . The boundary condition at $\mu = \mu_{j_{max}}$ fixes $a_{j_{max}} = 1$ (equation [27]).

After that the new timestep $\Delta t^{n+3/2}$ has been computed, the radial component of the fluid 4-velocity is calculated from the Euler equation (3) ($j_{min} + 1 \leq j \leq j_{max} - 1$)

$$\begin{aligned} u_j^{n+3/2} = u_j^{n+1/2} & - \Delta t^{n+1} a_j^{n+1} \left\{ \frac{\Gamma_j}{h_j} \left[\frac{8\pi r_j^2}{1 + \alpha} \left(\frac{p_{j+1/2} - p_{j-1/2}}{\Delta\mu_{j-1/2}} \right) + \frac{(s_1)_j}{\rho_j} \right] + \right. \\ & \left. + 4\pi r_j \left[p_j + \left(\frac{1}{3} + f_j \right) (w_0)_j \right] + \frac{M_j}{r_j^2} \right\}^{n+1}, \end{aligned} \quad (\text{A11})$$

where Δt^{n+1} is defined below (equation [A19]) and Γ_j , h_j , p_j , ρ_j and f_j have been radially interpolated using equation (A1). Along with w_1 , also the effective gravitational mass M has been linearly extrapolated in time at level t^{n+1} . At this point u_j^{n+1} can be interpolated from $u_j^{n+1/2}$ and $u_j^{n+3/2}$ and the value of Γ_j^{n+1} can be updated. The inner and outer boundary conditions for u are (equations [29] and [30])

$$u_{j_{min}}^{n+3/2} = u_{j_{min}}^{n+1/2} + \Delta t^{n+1} a_{j_{min}}^{n+1} \frac{M_{j_{min}}^{n+1}}{(r_{j_{min}}^{n+1})^2} \quad (\text{A12})$$

$$u_{j_{max}}^{n+3/2} = u_{j_{max}}^{n+1/2}, \quad (\text{A13})$$

where $a_{j_{min}}^{n+1}$ has been radially extrapolated from the neighboring mesh points.

The first moment of the specific intensity is computed from equation (24). In finite difference form it reads ($j_{min} + 1 \leq j \leq j_{max} - 1$)

$$(w_1)_j^{n+3/2} = \frac{1}{1 + F_w/2} \left[\left(1 - \frac{F_w}{2} \right) (w_1)_j^{n+1/2} + H_w \right], \quad (\text{A14})$$

where

$$F_w = \Delta t^{n+1} a_j^{n+1} \left[(k_R)_j \rho_j + \frac{2}{r_j} \frac{u_{j+1/2} r_{j+1/2} - u_{j-1/2} r_{j-1/2}}{r_{j+1/2} - r_{j-1/2}} \right]^{n+1} \quad (\text{A15})$$

$$H_w = \Delta t^{n+1} \left\{ \frac{8\pi a_j r_j}{\Gamma_j} (w_1)_j^2 - a_j \Gamma_j \left[\frac{(1/3 + f_{j+1/2}) (w_0)_{j+1/2} - (1/3 + f_{j-1/2}) (w_0)_{j-1/2}}{r_{j+1/2} - r_{j-1/2}} \right] - \Gamma_j \left(\frac{4}{3} + f_j \right) (w_0)_j \frac{a_{j+1/2} - a_{j-1/2}}{r_{j+1/2} - r_{j-1/2}} - 3 \frac{a_j \Gamma_j}{r_j} f_j (w_0)_j \right\}^{n+1}. \quad (\text{A16})$$

As in the 0–th moment equation, to derive equation (A14) we have expressed $r_{,t}$ and $b_{,t}/b = -(\rho r^2)_{,t}/\rho r^2$ using equations (8) and (4). To evaluate the radiation self-gravity term (the first term in curly brackets in equation [A16]) an extrapolated value (in time) of w_1 is used. The inner boundary condition is a 5 point Lagrangian extrapolation in radius. Following Mihalas & Mihalas (1984) and Shapiro (1996), we impose the outer boundary condition applying equation (24) across the half-zone from $j_{max} - 1/2$ to j_{max} and substituting $(w_1)_{j_{max}} = g(w_0)_{j_{max}}$ for $(w_0)_{j_{max}}$ in the gradients with respect to μ . The closure boundary factor g is given by equation (13).

Finally, the last quantity to be computed is the gravitational mass M . Integrating equation (7) along the time slice at constant t , we obtain ($j_{min} + 1 \leq j \leq j_{max}$)

$$M_j^{n+1} = M_{j-1}^{n+1} + \frac{4\pi (r^2)_{j-1/2}^{n+1}}{r_j^{n+1} - r_{j-1}^{n+1}} \left[\rho_{j-1/2} (1 + \epsilon_{j-1/2}) + (w_0)_{j-1/2} + \frac{u_{j-1/2}}{\Gamma_{j-1/2}} (w_1)_{j-1/2} \right]^{n+1}. \quad (\text{A17})$$

The boundary condition at $\mu = \mu_{j_{min}}$ fixes $M_{j_{min}} = M_0$ (equation [28]; see main text for explanation).

The timestep is computed at each cycle before the integration of the Euler equation according to

$$\Delta t^{n+3/2} = \min \left[\Delta t_\rho, \Delta t_B, \Delta t_c, (1.2 \Delta t^{n+1/2}) \right] \quad (\text{A18})$$

$$\Delta t^{n+1} = \frac{1}{2} (\Delta t^{n+1/2} + \Delta t^{n+3/2}) \quad (\text{A19})$$

where ($j_{min} + 1 \leq j \leq j_{max}$)

$$\Delta t_\rho = \min \left[0.05 \frac{\rho_{j-1/2}^{n+1}}{\rho_{j-1/2}^{n+1} - \rho_{j-1/2}^n} \Delta t^{n+1/2} \right]$$

$$\Delta t_B = \min \left[0.1 \frac{B_{j-1/2}^{n+1}}{B_{j-1/2}^{n+1} - B_{j-1/2}^n} \Delta t^{n+1/2} \right]$$

$$\Delta t_c = \min \left[0.4 \frac{\Delta \mu_{j-1/2}}{4\pi \rho_{j-1/2}^{n+1} (r^2)_{j-1/2}^{n+1} a_{j-1/2}^{n+1} (v_c)_{j-1/2}^{n+1}} \right] \quad \text{Courant condition.}$$

Here $v_c = (f + 1/3)^{1/2}$ is the radiation characteristic speed (the fastest speed on the grid).

Artificial viscosity is inserted into the finite difference equations adding a scalar stress $q_{j-1/2}$ to the gas pressure $p_{j-1/2}$ (von Neumann & Richtmyer 1950):

$$q_{j-1/2} = 2\rho_{j-1/2} (u_j - u_{j-1})^2 \quad \text{if } u_{j-1} - u_j > 0 \quad (\text{A20})$$

$$= 0 \quad \text{otherwise.} \quad (\text{A21})$$

REFERENCES

- Arnett, D. 1980, *ApJ*, 237, 541
- Arnett, D. 1996, *Supernovae and Nucleosynthesis* (Princeton: Princeton University Press)
- Arnett, D., Bahcall, J.N., Kirshner, R.P., & Woosley, S.E. 1989, *ARA&A*, 27, 629
- Berger, M.J., & Olinger, J. 1984, *Journal of Computational Physics*, 53, 484
- Blondin, J.M. 1986, *ApJ*, 308, 755
- Brown, G.E., & Bethe, H.A. 1994, *ApJ*, 423, 659
- Burrows, A. 1988, *ApJ*, 334, 891
- Chen, K., & Colgate, S.A. 1995, *ApJ*, submitted
- Chernoff, D.F., Shapiro, S.L., & Wasserman, I. 1989, *ApJ*, 337, 814
- Chevalier, R.A. 1989, *ApJ*, 346, 847
- Chevalier, R.A. 1996, *ApJ*, 459, 322
- Christy, R.F. 1966, *ApJ*, 144, 108
- Colgate, S.A. 1971, *ApJ*, 163, 221
- Colgate, S.A. 1988, in *Supernova 1987 A in the Large Magellanic Cloud*, ed. M. Kafatos and G. Michalitsianos (Cambridge: Cambridge University Press), 341
- Colpi, M., Shapiro, S.L., & Wasserman, I. 1996, *ApJ*, 470, 1075 (CSW)
- Cordes, J., & Chernoff, D. 1997, *ApJ*, in press
- Dar, A. 1997, in the *Proceedings of the 1997 Rencontre de Physique de la Vallee d’Aoste*, in press
- Hansen, B.M.S., & Sterl Phinney, E. 1997, *MNRAS*, in press
- Houck, J.C., & Chevalier, R.A. 1991, *ApJ*, 376, 234
- Hummer, D.G., & Rybicki, G.B. 1971, *MNRAS*, 152, 1
- Kunkel, W., Madore, B., Shelton, I.K., Dihalde, O., Bateson, F. M., Jones, A., Moreno, B., Walker, S., McNaught, R.H., Garradd, G., Warner, B., & Menzies, J. 1987, *IAU Circular No. 4316*
- Lattimer, J.M., & Swesty, F.D. 1991, *Nucl. Phys. A*, 535, 331
- May, M.M., & White, R.H. 1967, in *Methods in Computational Physics*, Vol. 7 (New York: Academic Press), 219
- McCray, R. 1993, *ARA&A*, 31, 175
- McCray, R., Shull, J.M., & Sutherland, P. 1987, *ApJ*, 317, L73
- Mihalas, D., & Weibel Mihalas, B. 1984, *Foundations of Radiation Hydrodynamics* (Oxford: Oxford University Press)
- Nobili, L., Turolla, R., & Zampieri, L. 1991, *ApJ*, 383, 250
- Pandharipande, V.R. 1997, in the *Proceedings of the Xth International Conference on Recent Progress in Many-Body Theories*, ed. D. Nelson (Singapore: World Scientific Publishing), in press
- Park, M.-G. 1990, *ApJ*, 354, 64
- Rezzolla, L., & Miller, J.C. 1994, *Class. Quantum Grav.*, 11, 1815
- Rybicki, G.B., & Lightman, A.P. 1979, *Radiative Processes in Astrophysics* (New York: Wiley)

- Shapiro, S.L. 1996, ApJ, 472, 308
- Suntzeff, N.B. 1997, in SN1987A: Ten Years After, ed. M.M. Phillips and N.B. Suntzeff (ASP Conference Series), in press
- Thorsson, V., Prakash, M., & Lattimer, J.M. 1994, Nucl. Phys. A, 572, 693
- von Neumann, J., & Richtmyer, R.D. 1950, J. Appl. Phys., 21, 232
- Wilson, J.R., Mayle, R., Woosley, S.E., & Weaver T.A. 1986, in Proceedings of the 12th Texas Symposium on Relativistic Astrophysics, ed. M. Livio & G. Shaviv (New York: New York Academy of Sciences), 267
- Woosley, S.E. 1988, ApJ, 330, 218
- Woosley, S.E., & Weaver T.A. 1986, ARA&A, 24, 205
- Woosley, S.E., & Weaver T.A. 1995, ApJS, 101, 181
- Woosley, S.E., & Timmes, F.X. 1996, Nucl.Phys. A, 606, 137
- Zampieri, L. 1995, PhD thesis
- Zampieri, L. 1997, in the Proceedings of the Second International Sakharov Conference on Physics, ed. I.M. Dremin & A.M. Semikhatov (Singapore: World Scientific Publishing), in press
- Zampieri, L., Miller, J.C., & Turolla, R. 1996, MNRAS, 281, 1183

Fig. 1.— Light curve for model I. The observed luminosity $l = L/L_{Edd}$ is plotted versus time t in units of the initial accretion timescale $t_{a,0}$. The *squares* are the points computed numerically, while the *solid line* represents the analytic solution by Arnett (1980). The arrow marks the diffusion timescale t_{diff} .

Fig. 2.— Light curve for model II. The conventions and symbols are the same as in Figure 1.

Fig. 3.— Evolution of the accretion luminosity and accretion rate at a fixed radius $r_0 = 0.3r_{a,0}$, where $r_{a,0} = GM_{bh}/c_{s,0}^2$ is the initial accretion radius, for model II. (a) Luminosity $l(r_0)$ versus time t . (b) Accretion rate $\dot{m} = \dot{M}_0/\dot{M}_{Edd}$ versus time t .

Fig. 4.— Properties of the flow at selected times for model II. (a) Radial component of the 4-velocity $|u|$ in units of the initial sound velocity $c_{s,0}$ versus radius r in units of $r_{a,0}$. The dashed line denotes negative values. (b) Density ρ in units of the initial density ρ_0 versus radius. (c) Gas temperature T versus radius. (d) Luminosity l versus $r/r_{a,0}$. At the onset of evolution the radiative flux is taken to be zero. Curves are labeled by time in unit of $t_{a,0}$.

Fig. 5.— Light curve for model III. The conventions and symbols are the same as in Figure 1.

Fig. 6.— Luminosity l versus radius $r/r_{a,0}$ at selected times for model III.

Fig. 7.— Computed light curve for model IVa. The observed luminosity $l = L/L_{Edd}$ (*squares*) is plotted versus time t in units of the initial accretion timescale $t_{a,0}$. When recombination takes place ($t/t_{a,0} \sim 42$) the internal energy is released and the luminosity suddenly increases. After recombination the luminosity falls off exponentially until the emission is dominated by accretion (note the slow power law decline in l at late times).

Fig. 8.— Properties of the flow at selected times for model IVa. (a) Gas temperature T versus radius. Note the formation of the recombination front ($t/t_{a,0} \sim 42$) and its rapid inward motion. The front stalls as soon as it approaches the innermost accreting region. (b) Luminosity l versus $r/r_{a,0}$. (c) Radius of the recombination front r_{rec} as a function of $t/t_{a,0}$.

Fig. 9.— Light curve, effective temperature and photospheric temperature for model IVb. (a) Luminosity l (*squares*) versus time. (b) Effective temperature T_{eff} (*squares*), as defined by equation (48), and gas temperature at the photospheric radius T_{ph} (*circles*), as defined by equation (49), versus time.

Fig. 10.— Early evolution of model IVb. (a) Radial component of the 4-velocity $|u|$ versus radius r . The dashed line denotes negative values. Note the sign inversion of the velocity of the intermediate shells caused by the radiative force. (b) Luminosity l versus radius. The strong transient superEddington flux produced early in the evolution ($t \sim t_{a,0}$) pushes outwards the marginally bound shells near the accretion radius and then propagates outwards.

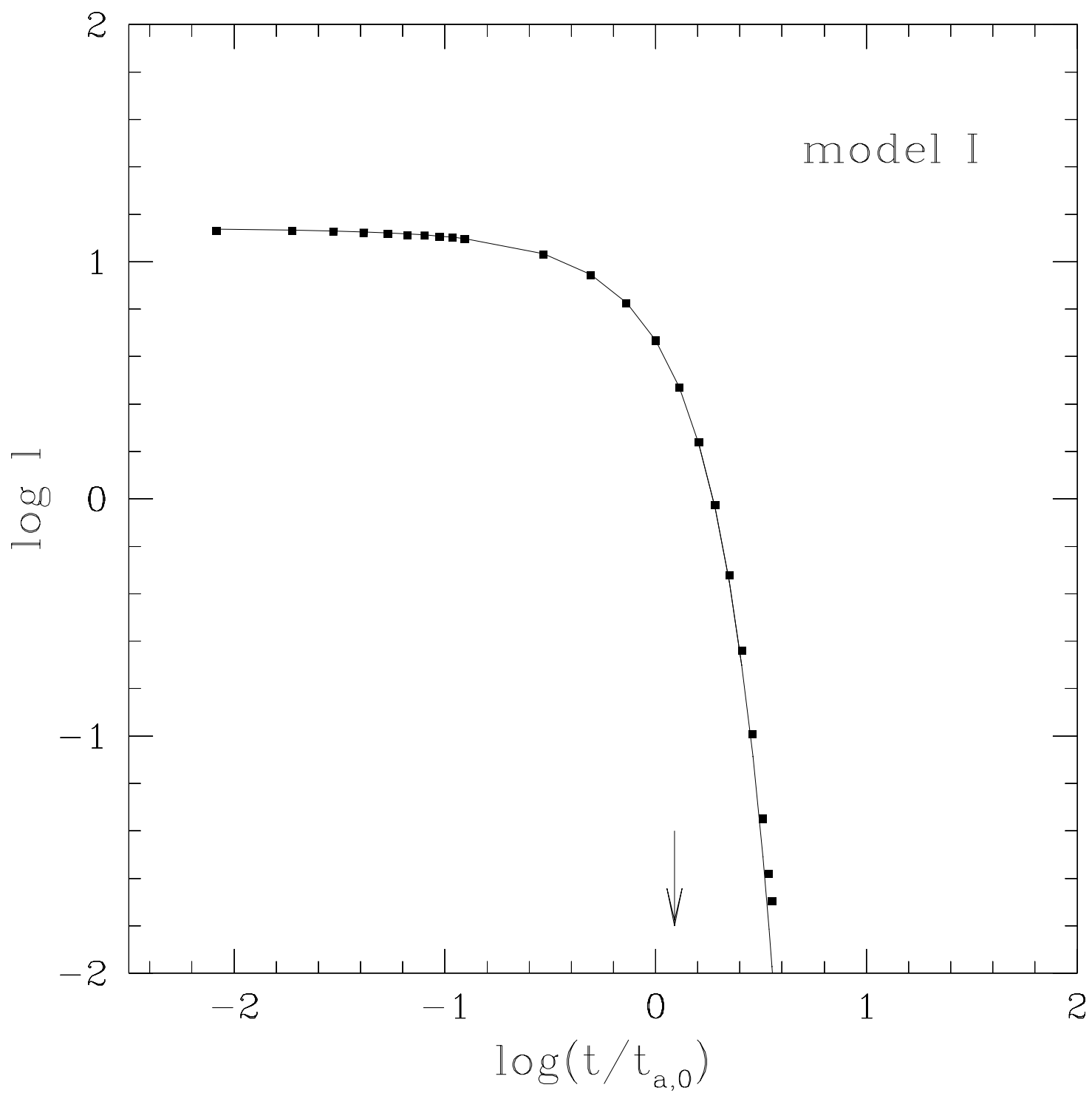
Fig. 11.— Accretion rate $\dot{m}(r_0)$ at a fixed radius ($r_0 = 0.1r_{a,0}$) versus time for model IVa (*squares*) and model IVb (*circles*).

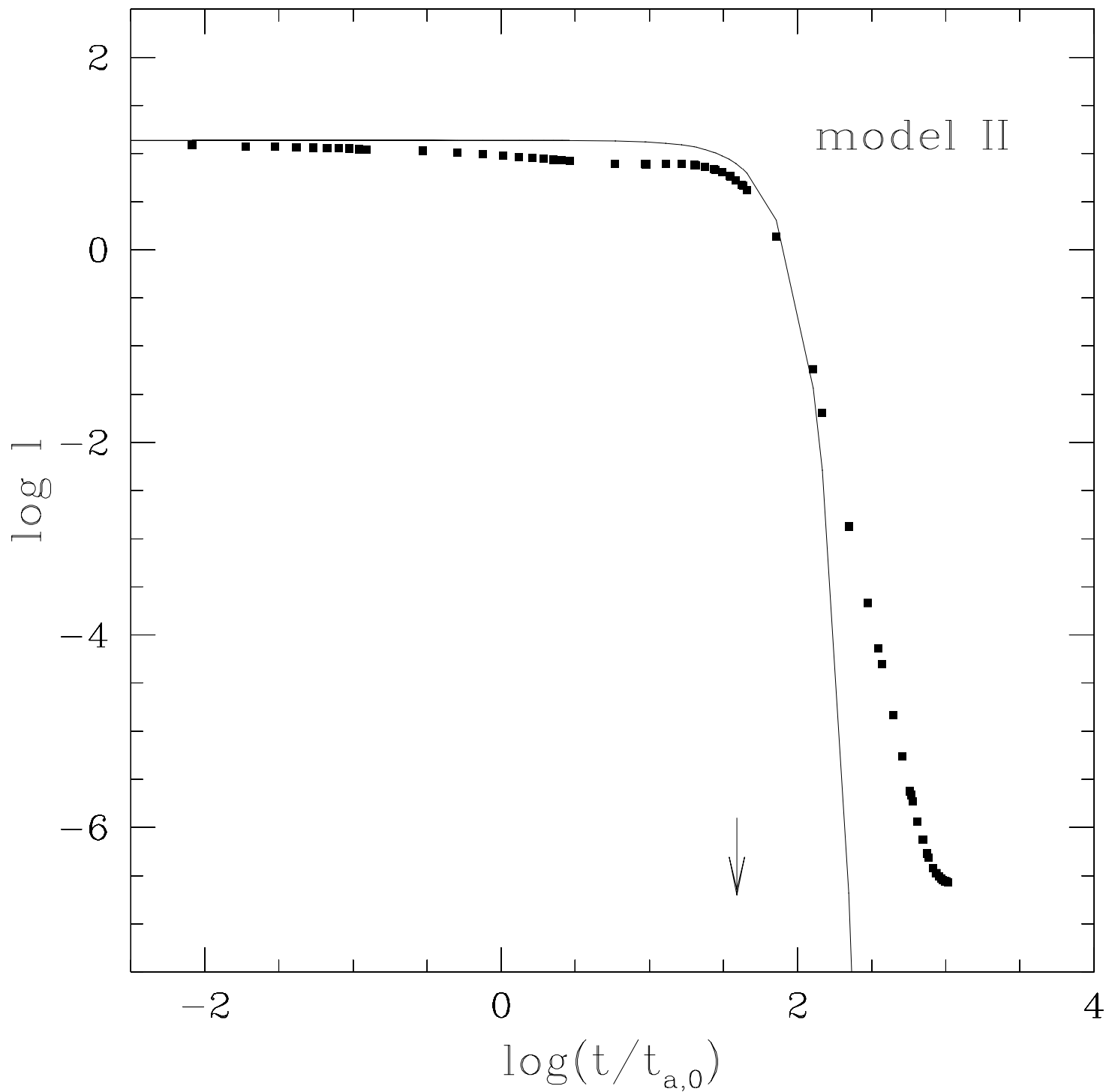
Fig. 12.— Mass flux \dot{m} versus radius at $t = 6 \times 10^3 t_{a,0}$ for model IVb. Note the constancy of \dot{m} with radius in the inner accreting region.

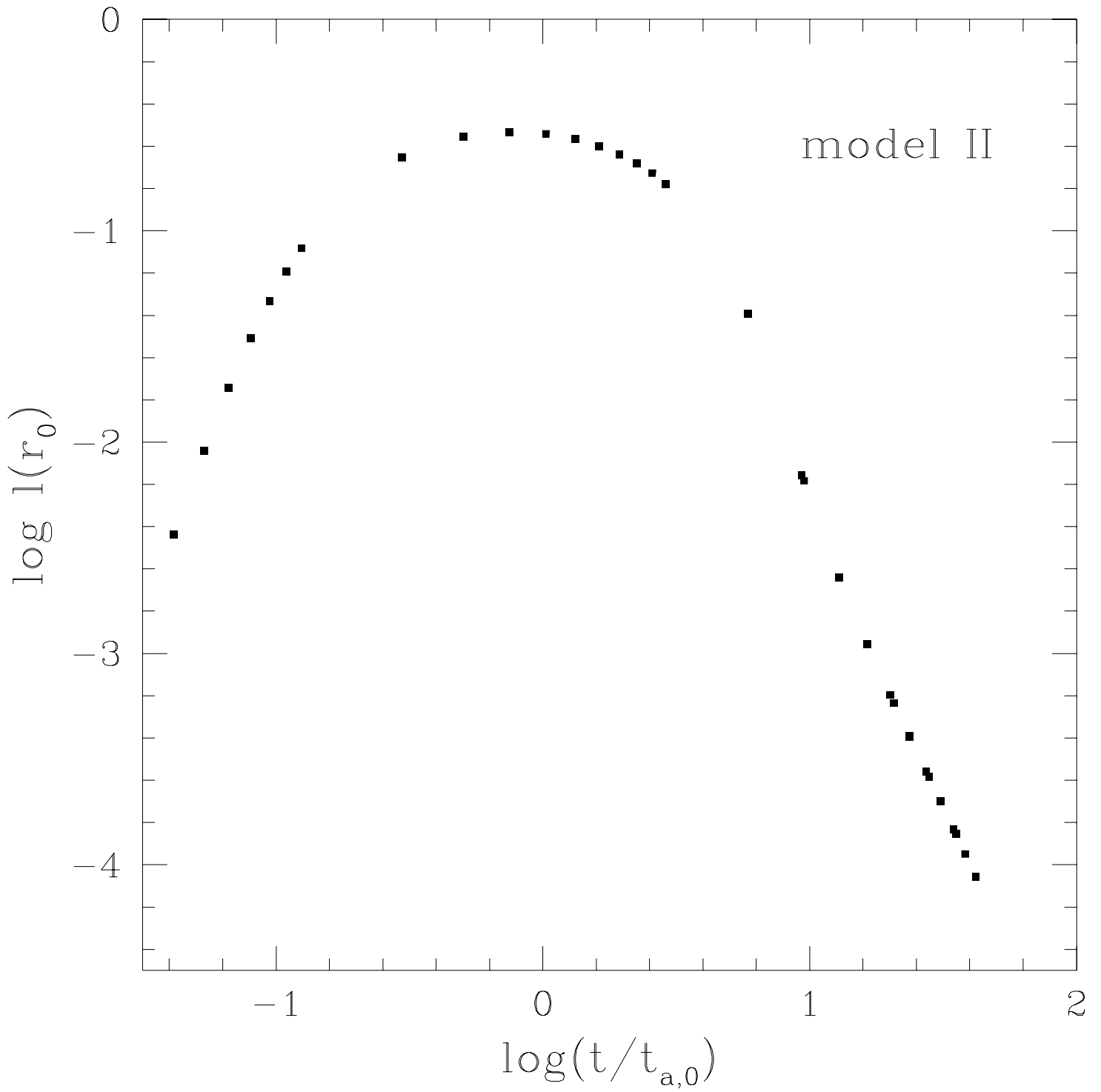
Fig. 13.— Tracks on the luminosity–accretion rate plane ($l-\dot{m}$) for model IVa and IVb. The observed luminosity l is plotted as a function of the accretion rate \dot{m} (evaluated in the inner accreting region). *Squares* denote the computed points for model IVa, while *circles* denote those of model IVb. The *solid line*

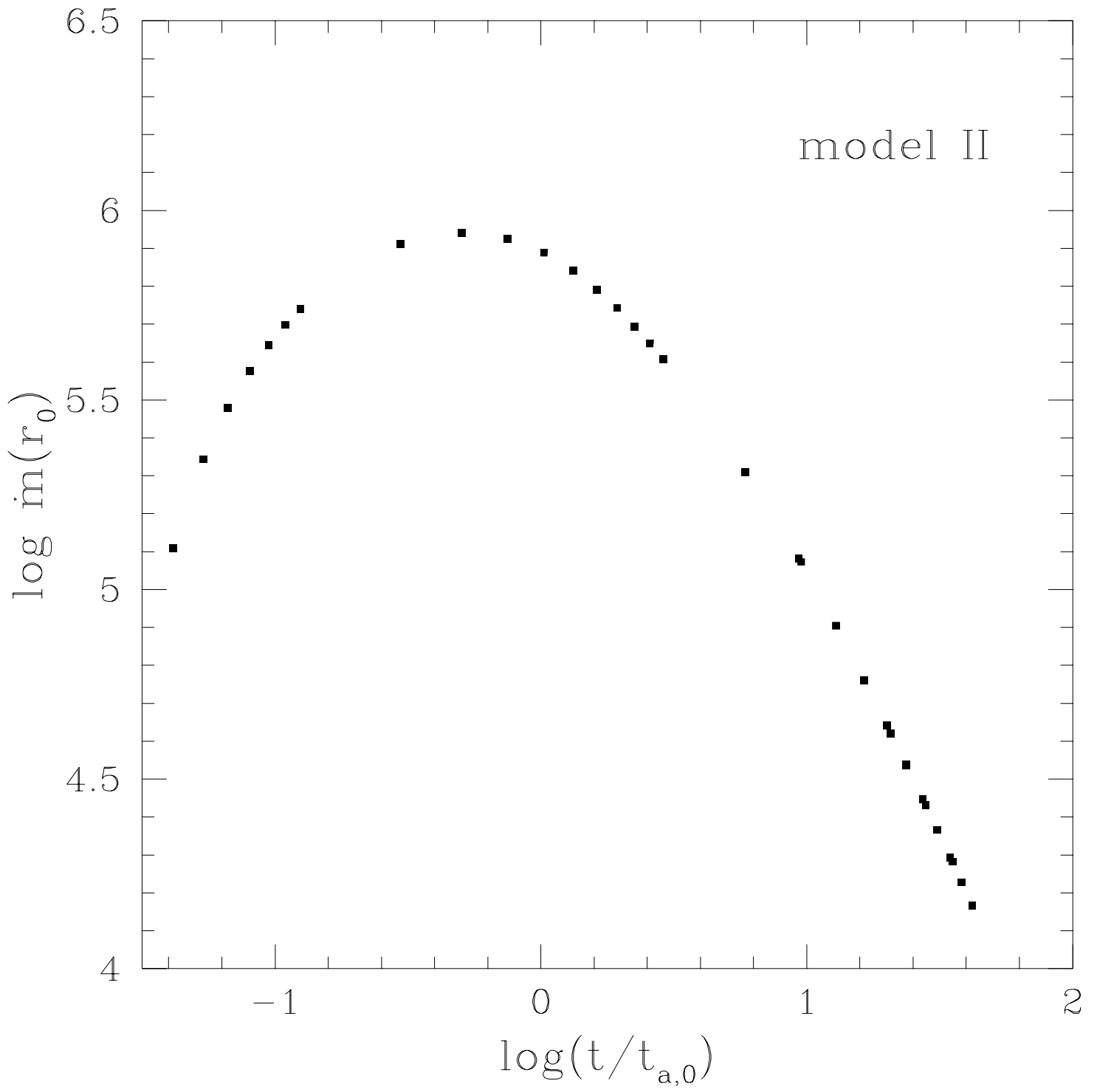
is the analytic expression of $l = l(\dot{m})$ for stationary models derived by Blondin (1986; see equation (52) in the main text).

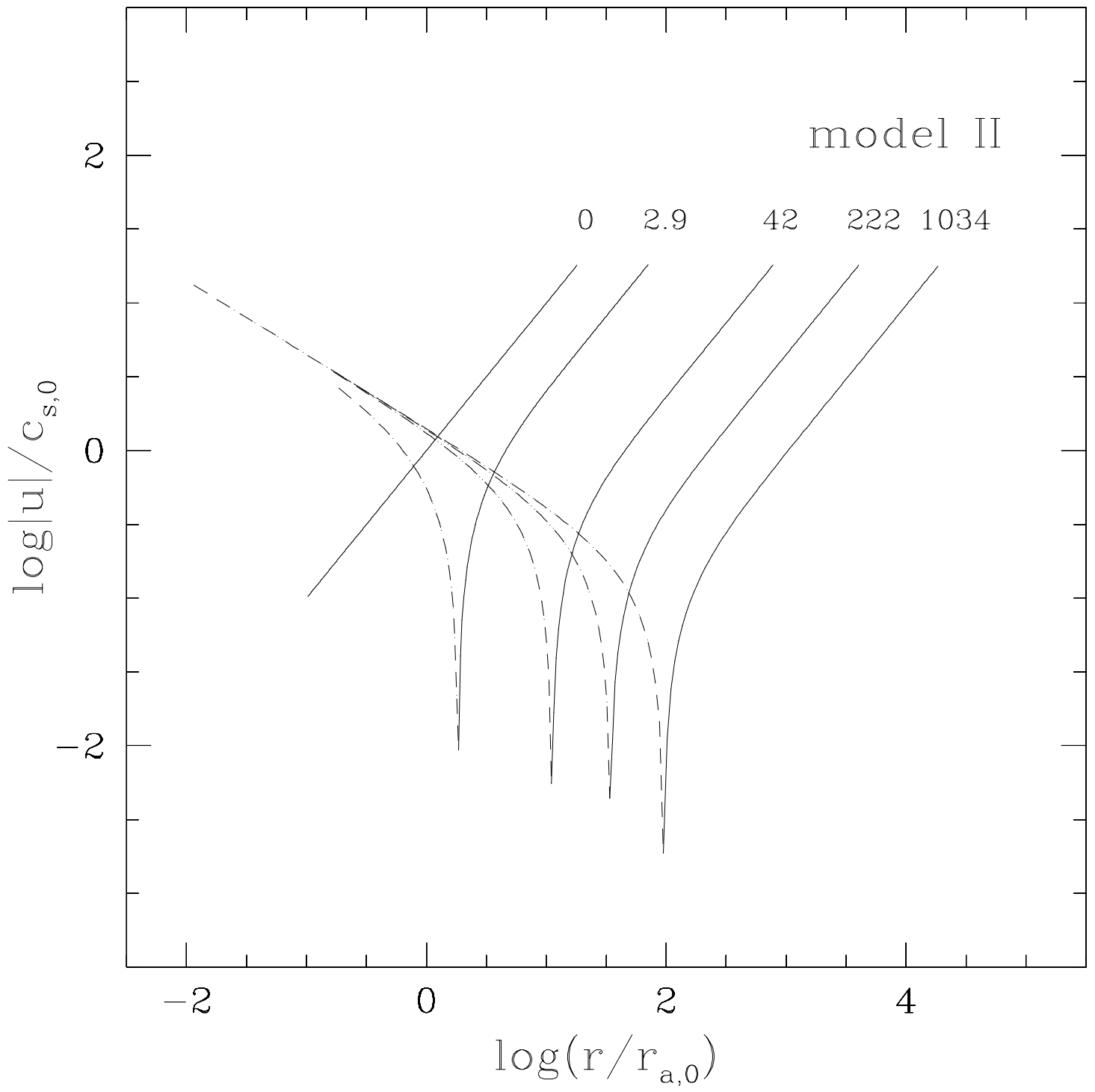
Fig. 14.— Computed and observed bolometric light curves for SN1987A. The luminosity L is plotted as a function of time t . *Squares (circles)* give the solution for model IVa (IVb). The *dotted lines* represent the extrapolation of the late-time evolution for the computed models (see Section 7). The *triangles* are the bolometric luminosity of SN1987A (data taken by McCray 1993, Woosley & Timmes 1996, Arnett 1996 and Suntzeff 1997). The *dashed lines* represent the expected contribution from the decay of radioactive elements ($0.07 M_{\odot}$ of ^{56}Co and $\sim 5 \times 10^{-5} M_{\odot}$ of ^{44}Ti). Finally, the *upper dotted line* denotes the expected bolometric luminosity emitted by a putative black hole in SN1987A. The *arrow* marks the time ($t \simeq 900$ years) at which the *upper dotted line* crosses the dashed line (radioactive emission from ^{44}Ti): from this moment on, the bolometric luminosity of SN1987A would be dominated by the energy released by accretion.

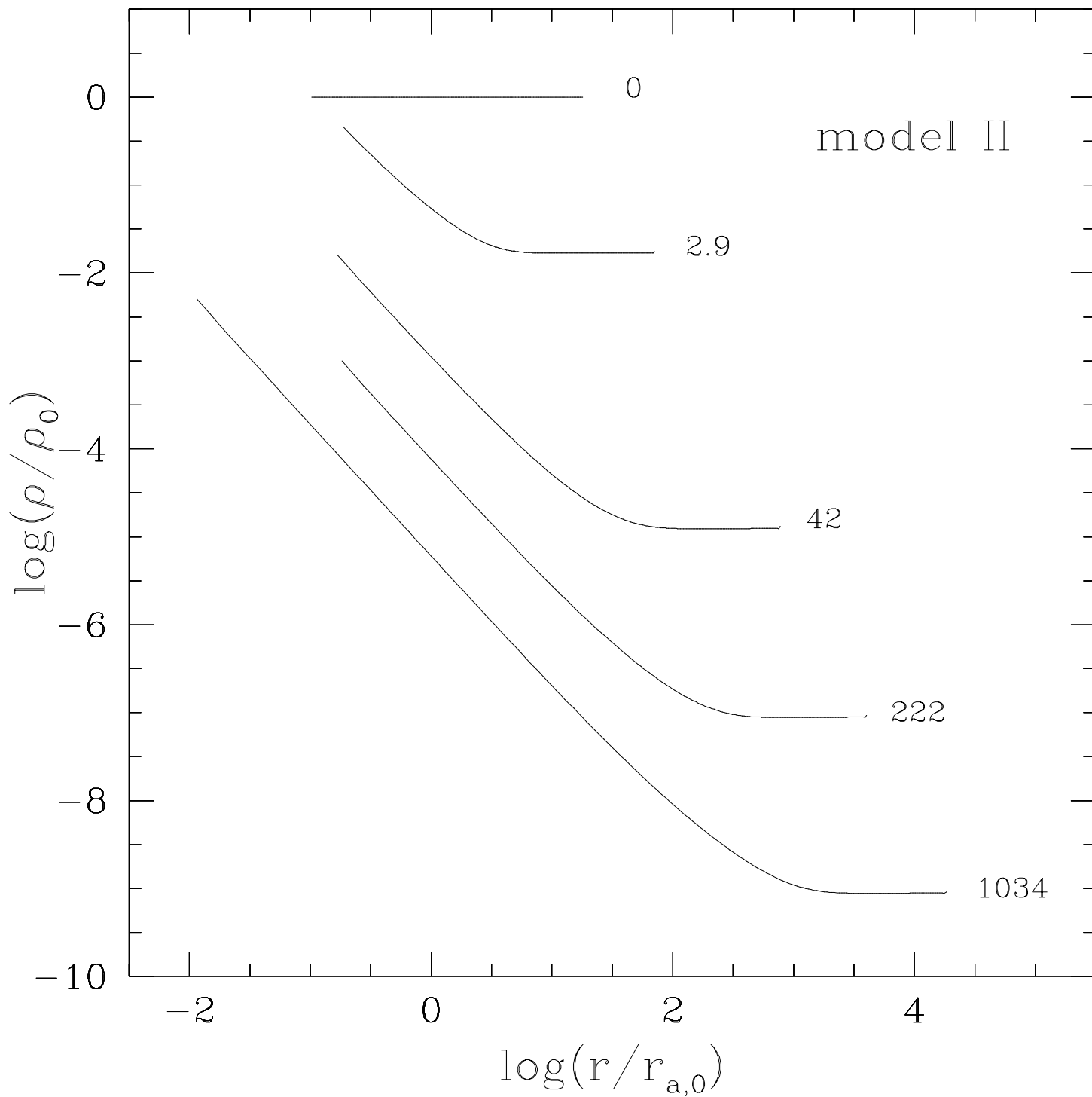


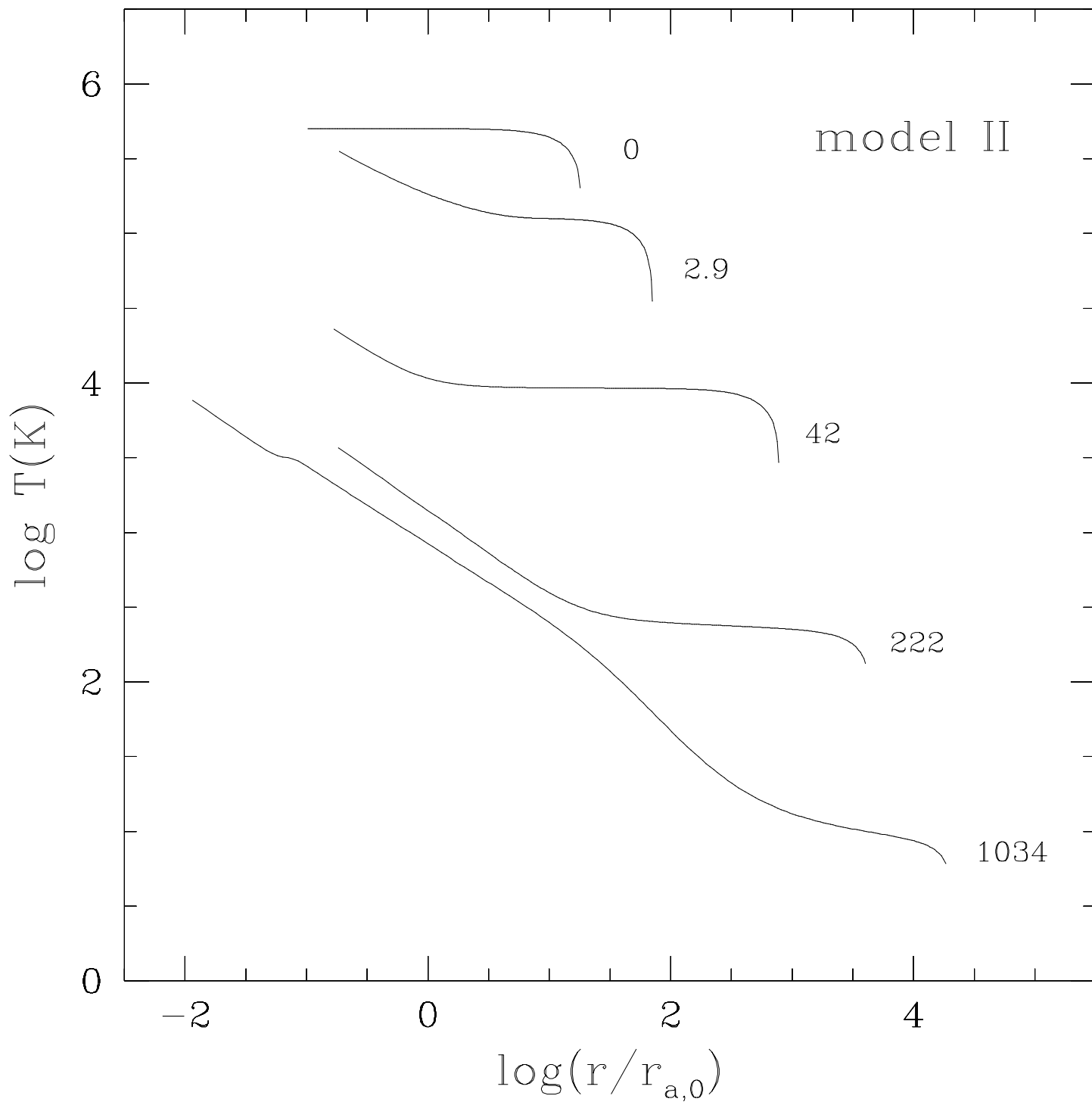


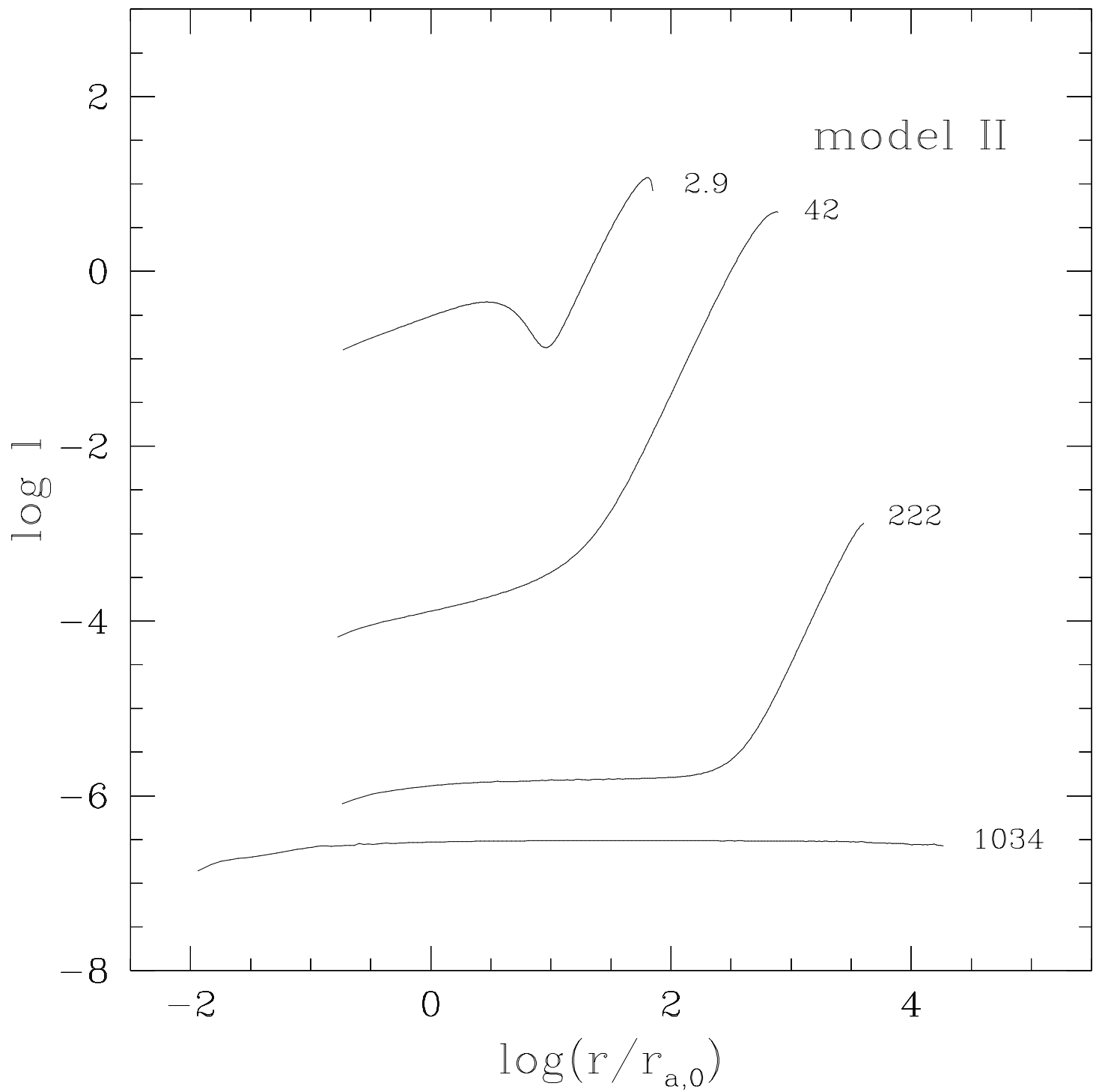


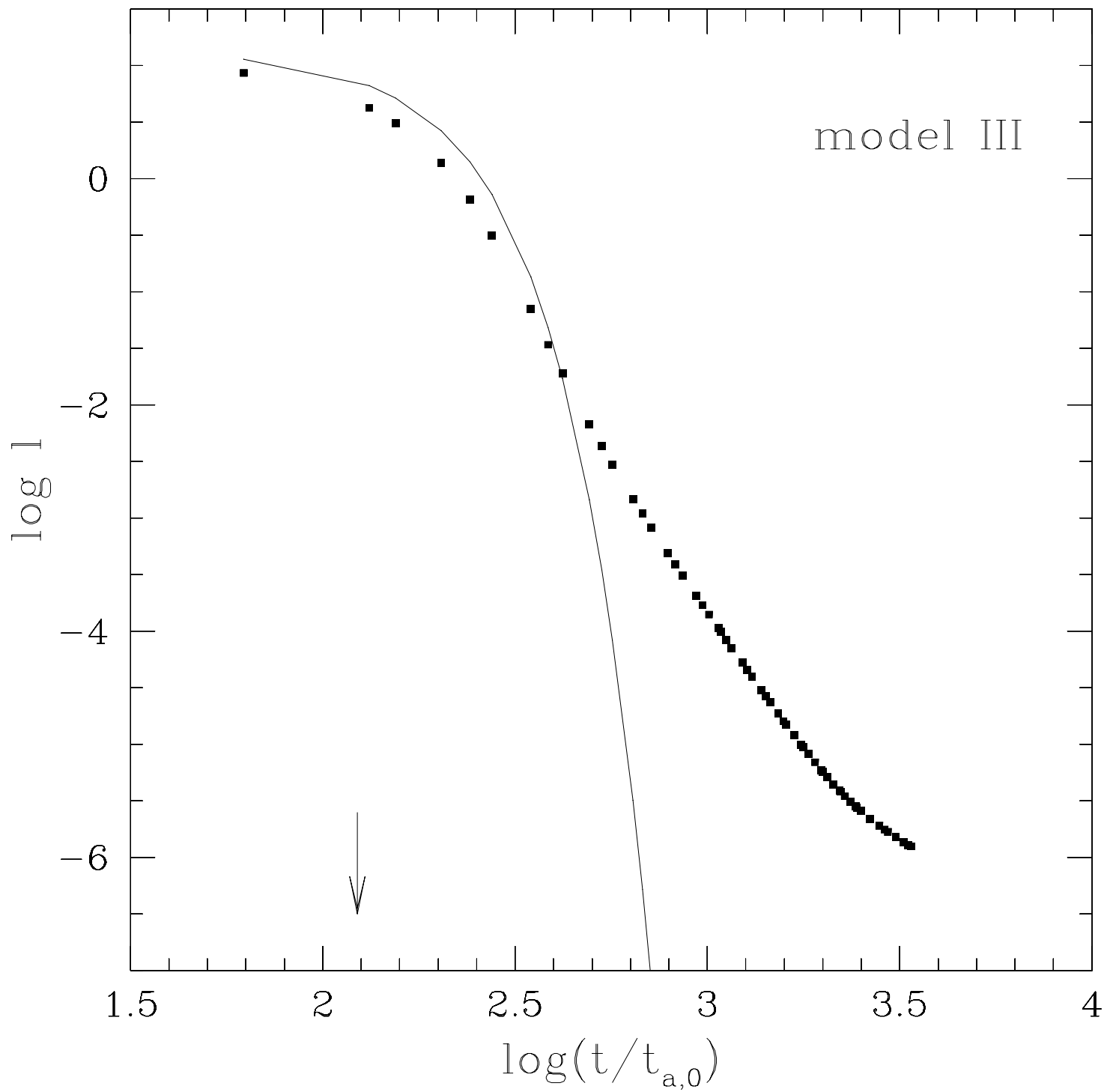


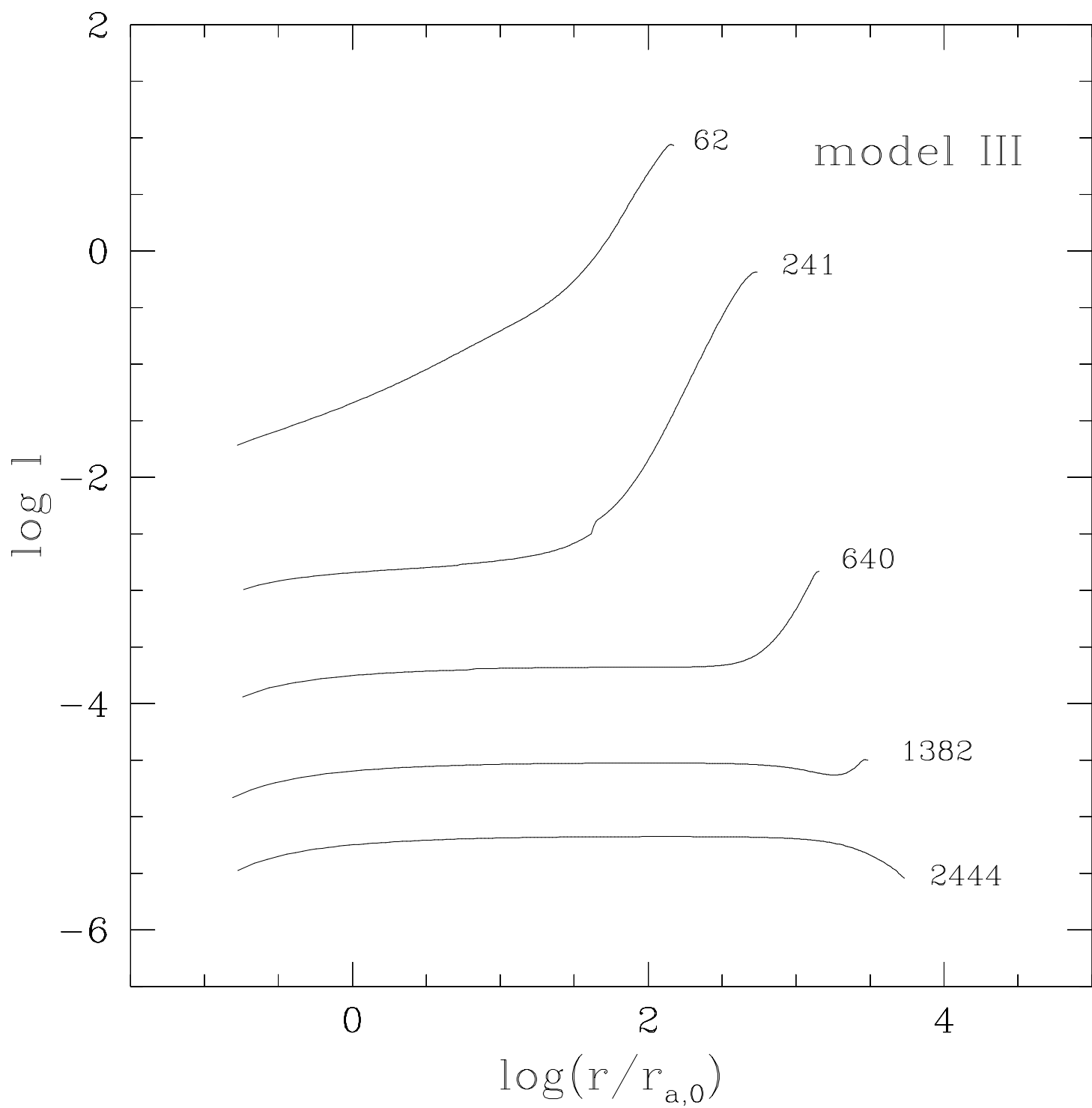


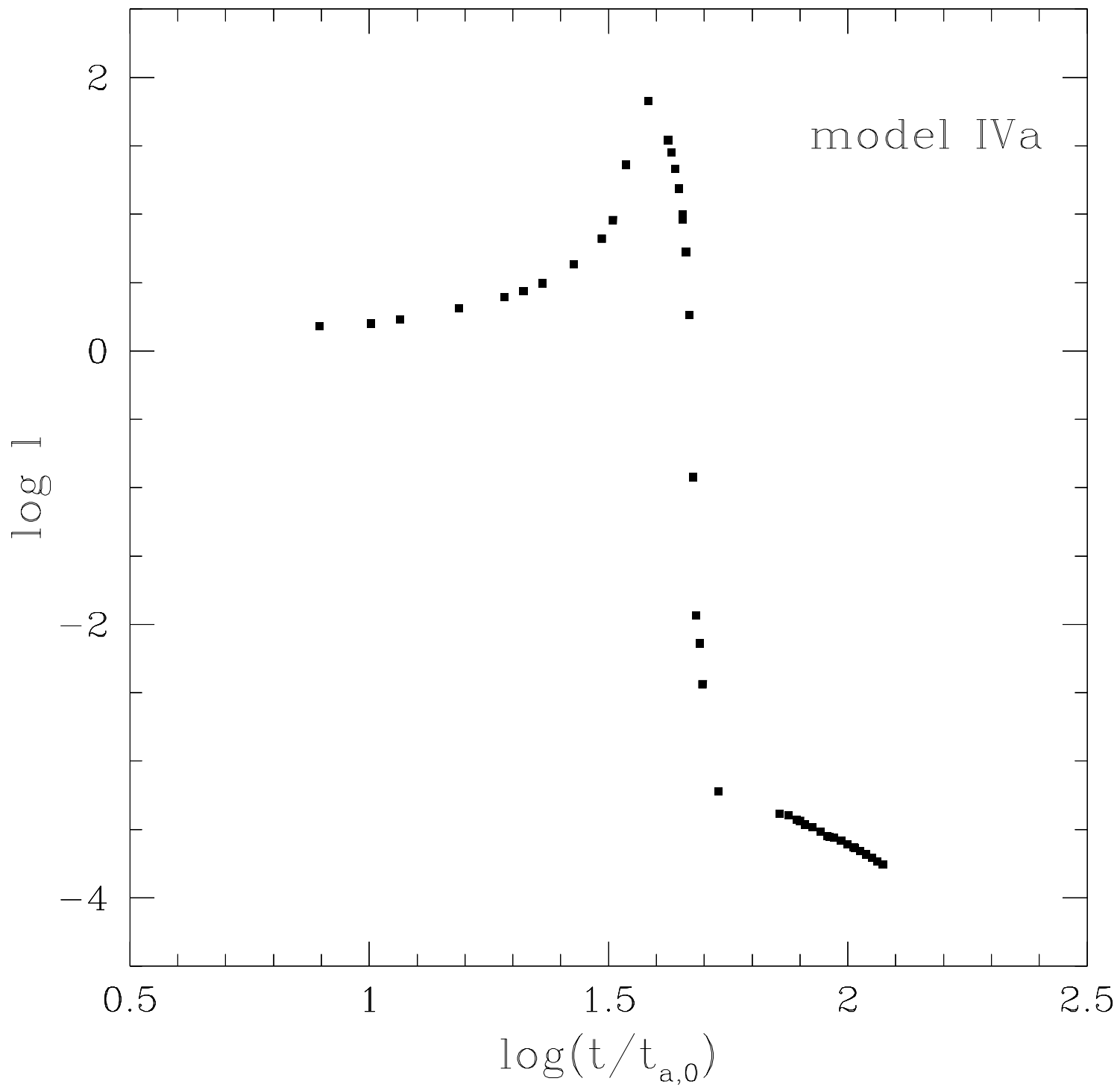


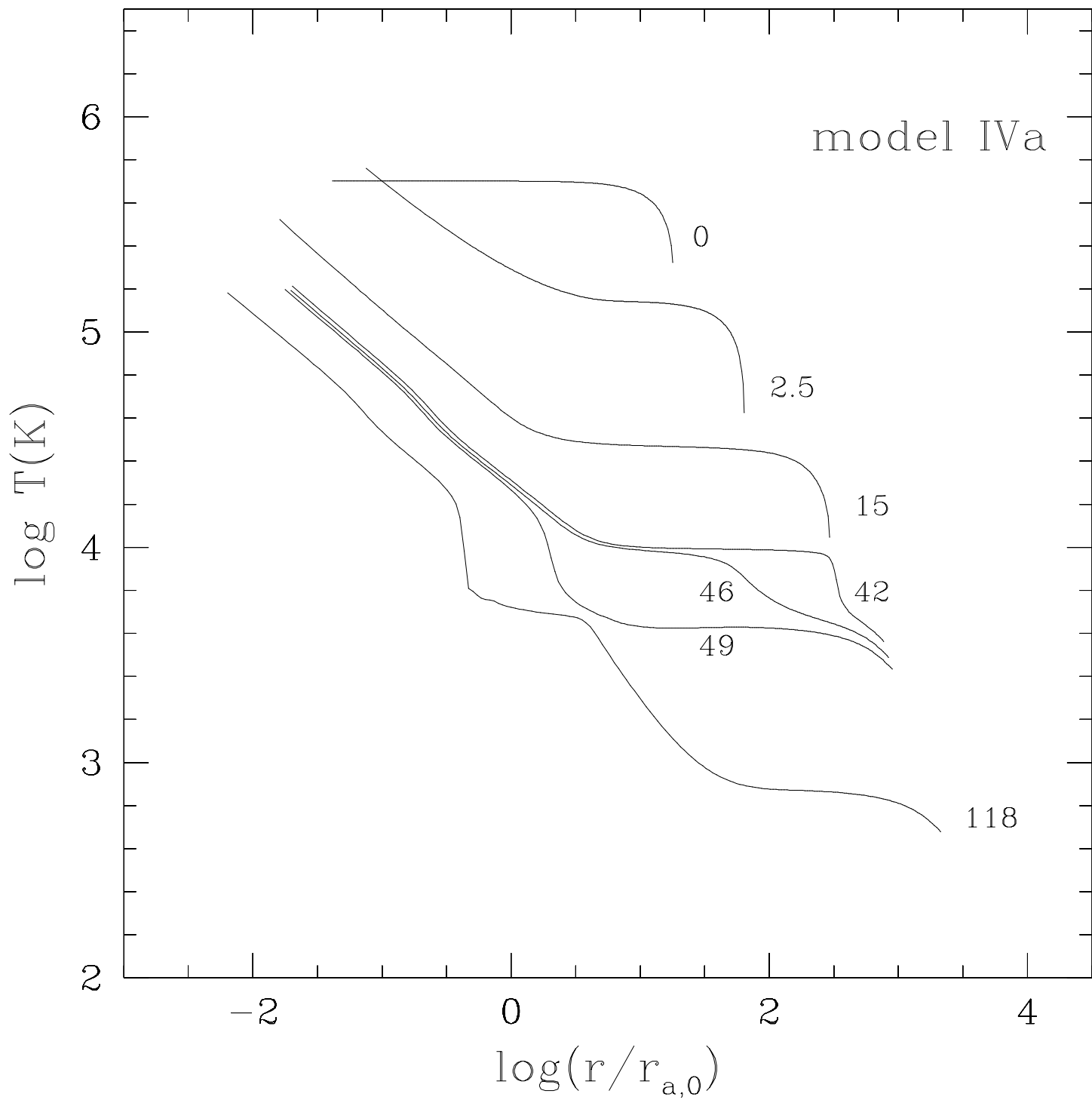


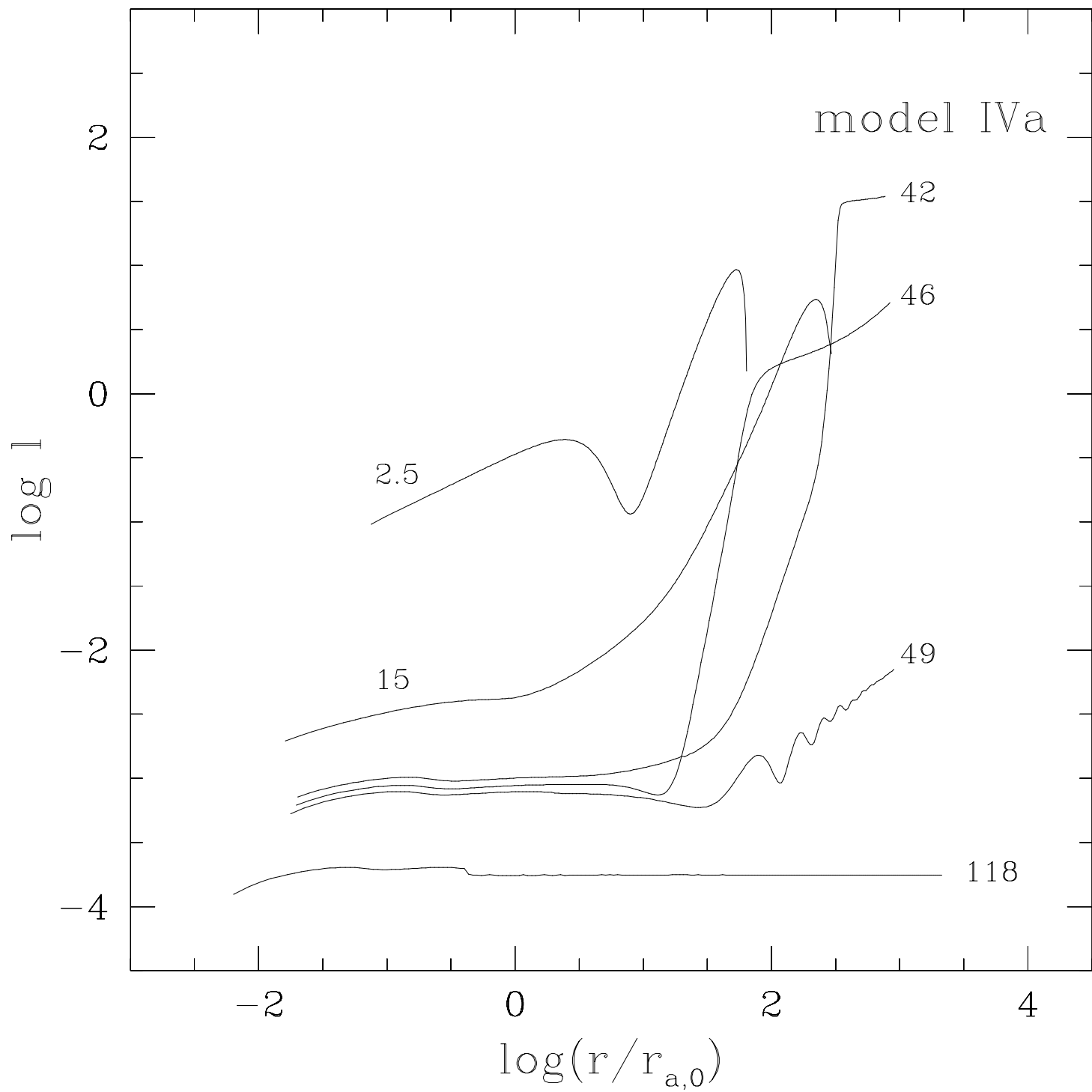


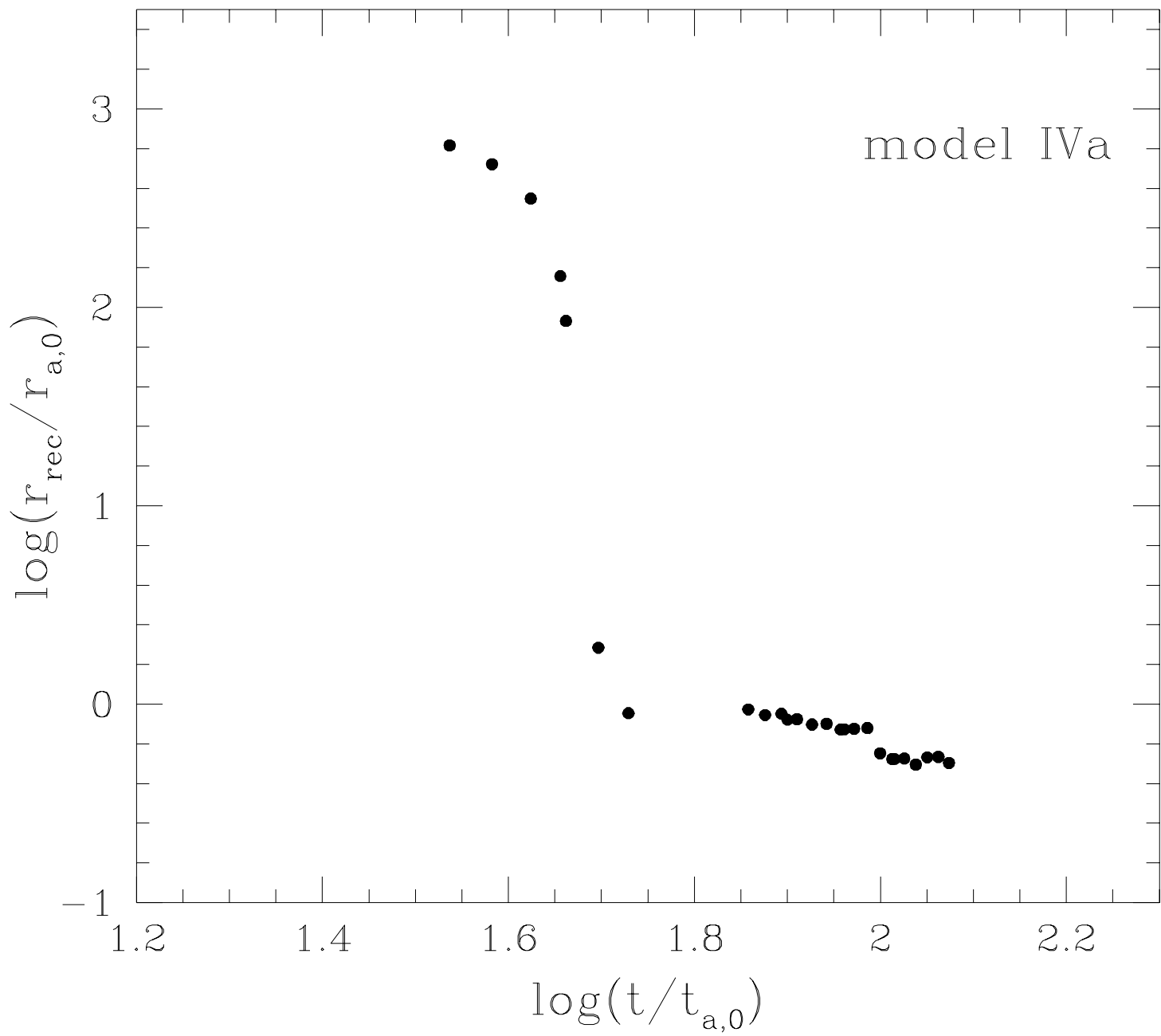


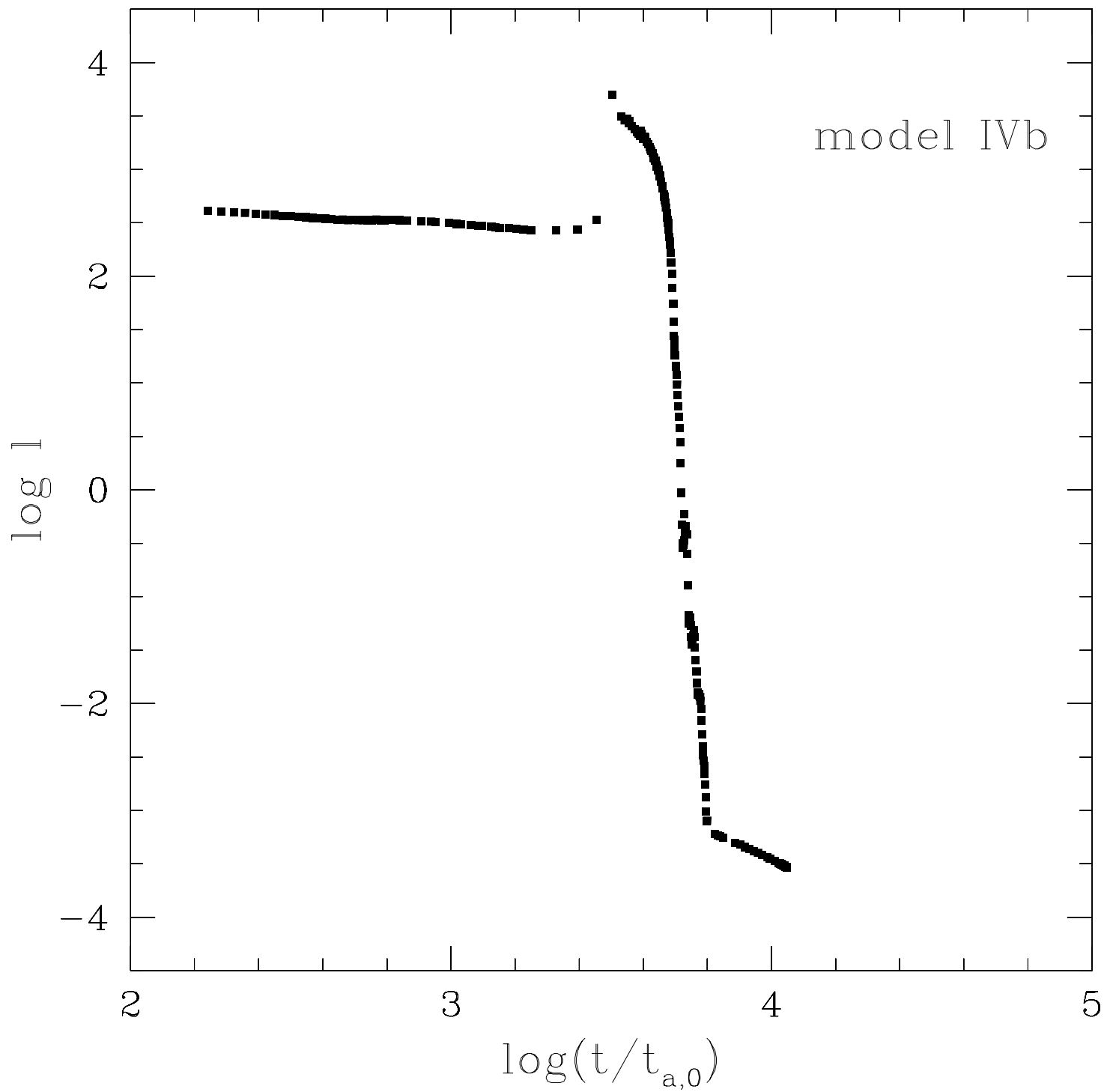


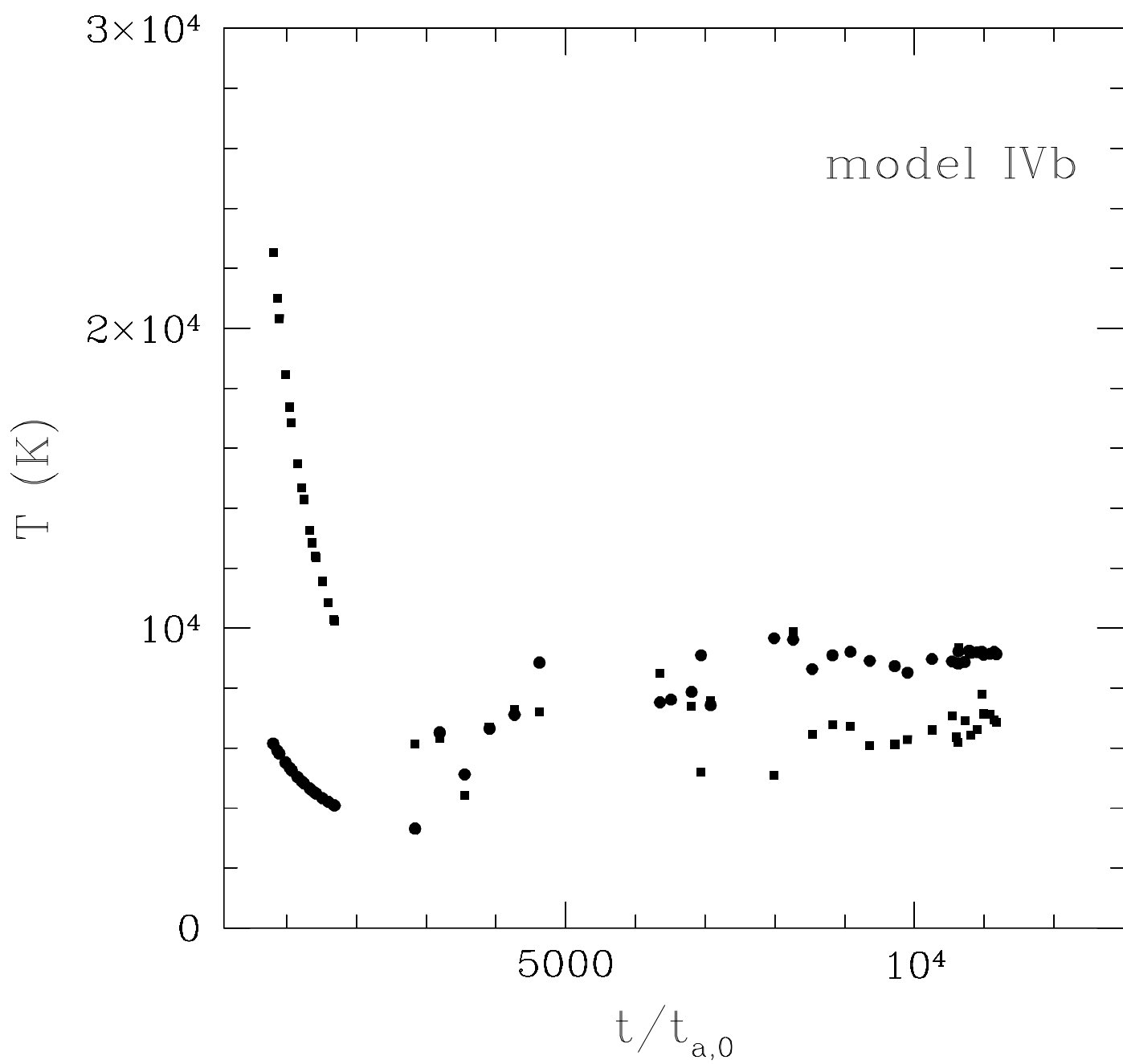


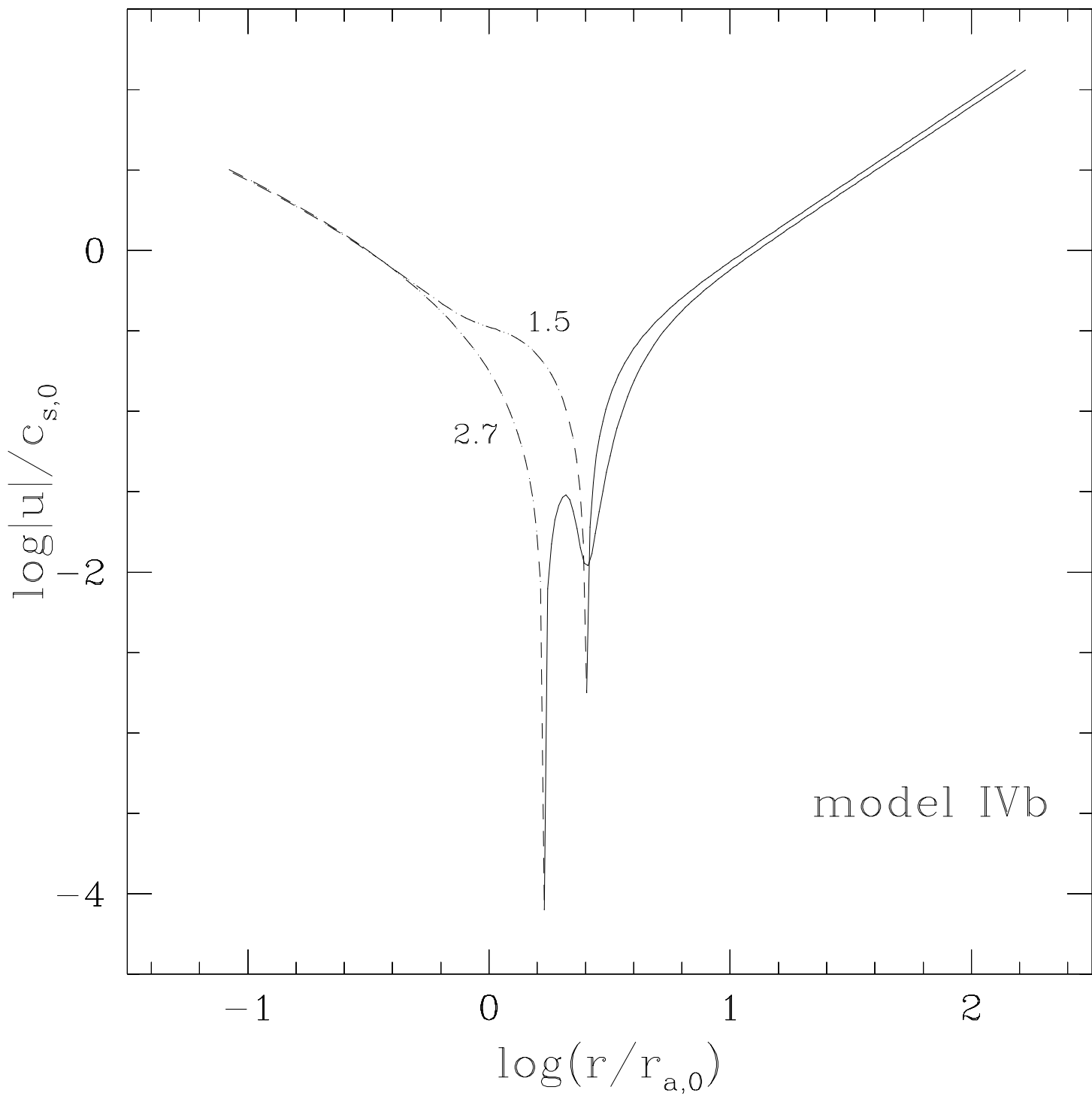


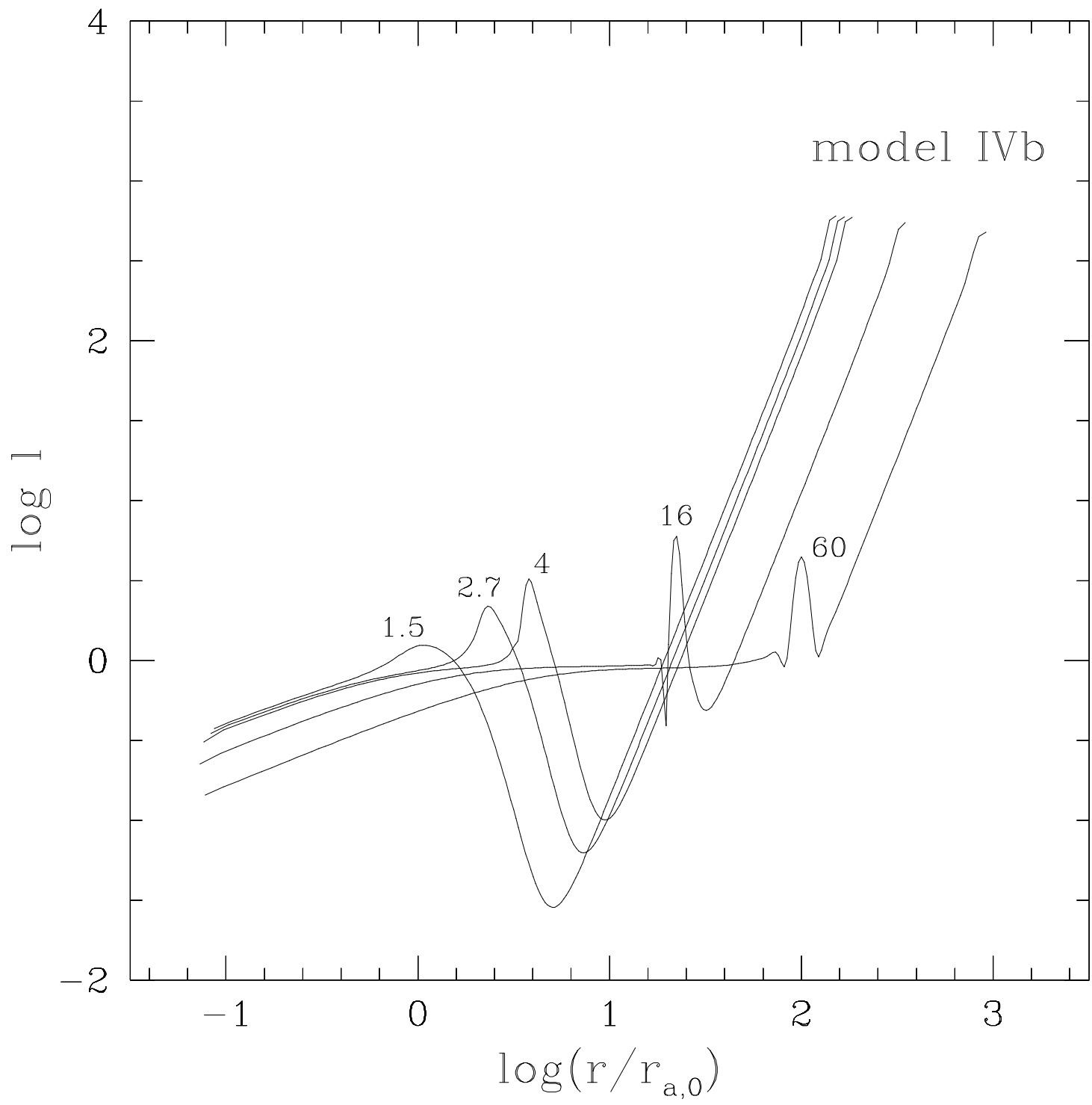


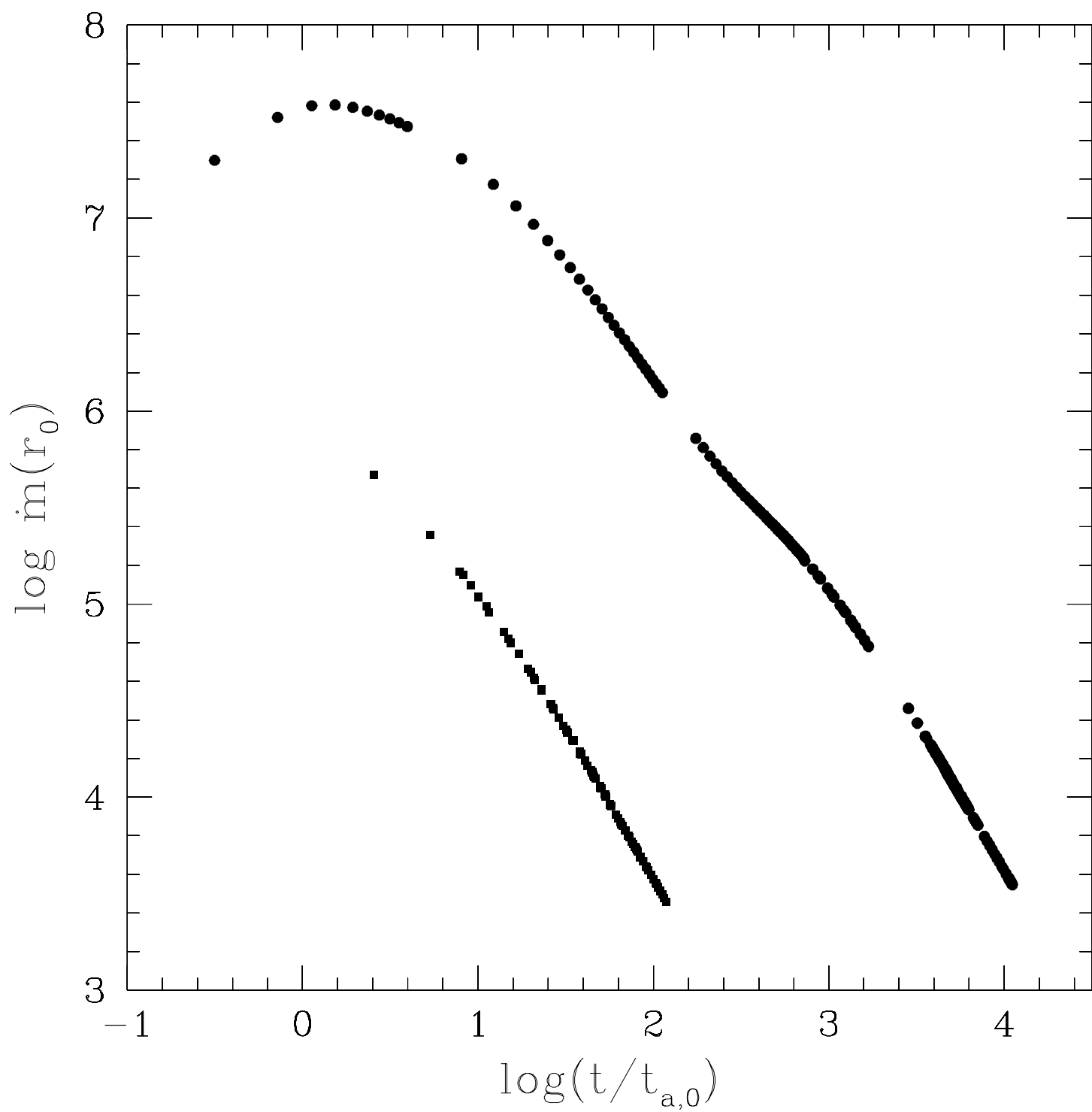


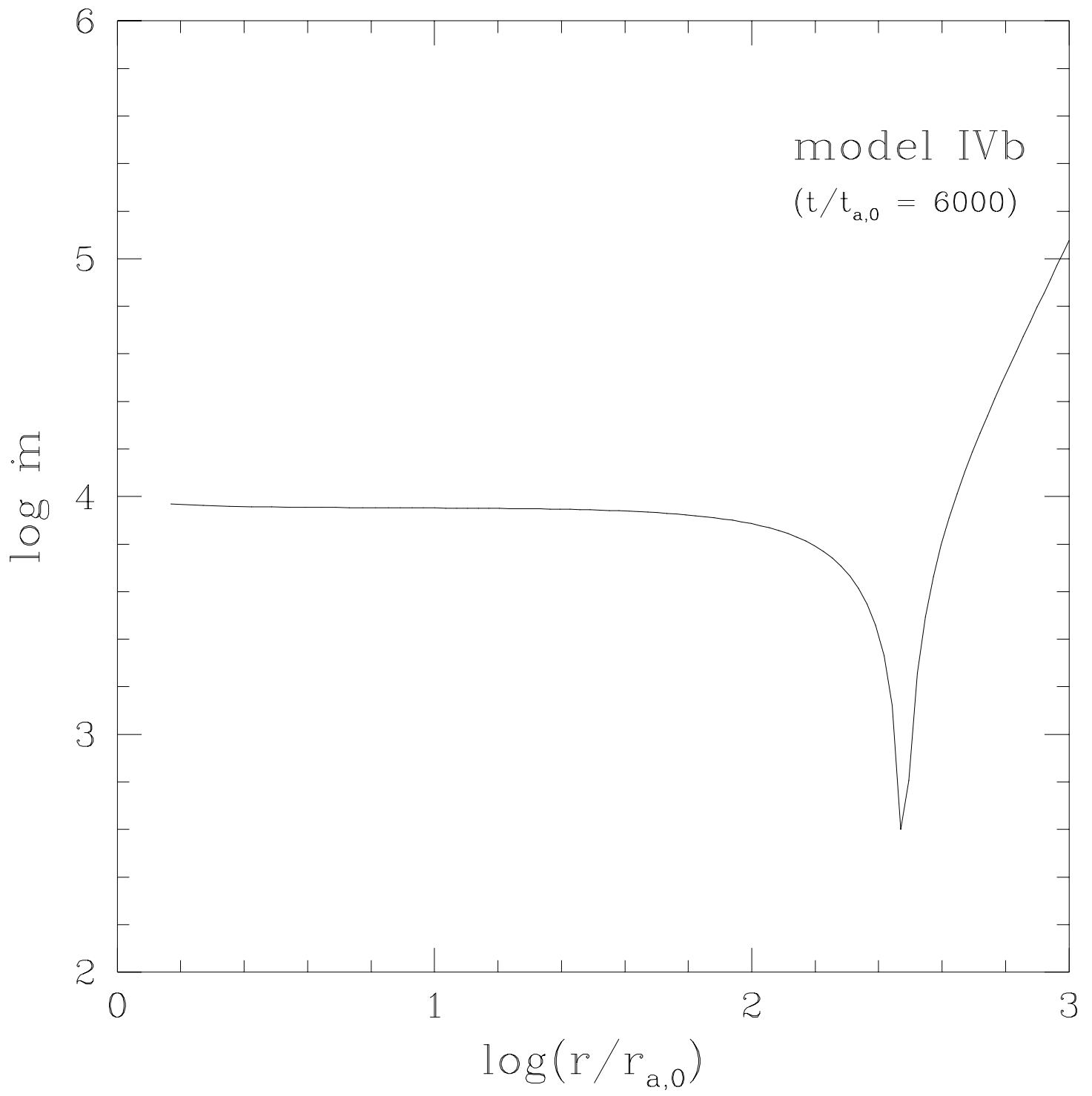


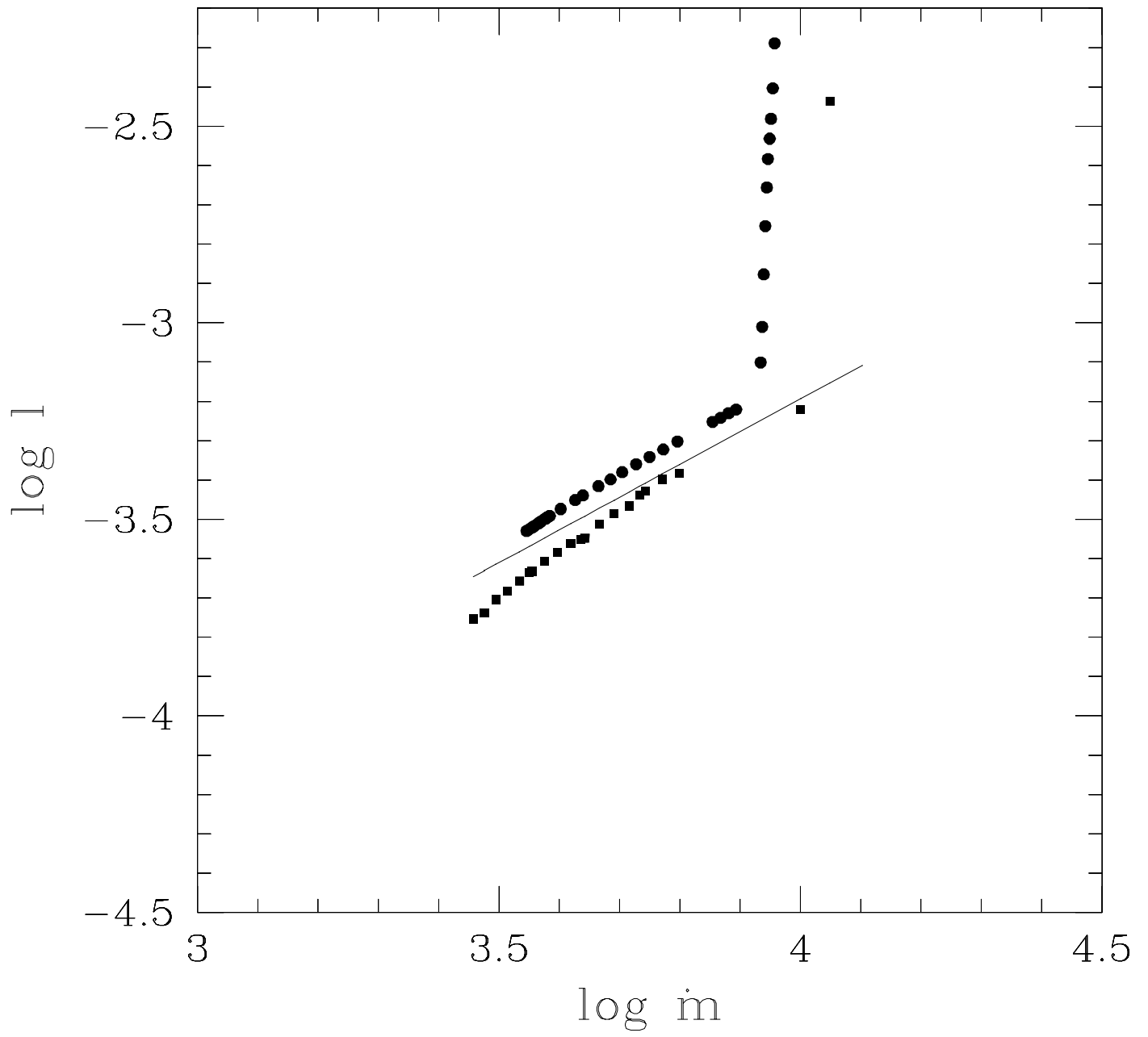












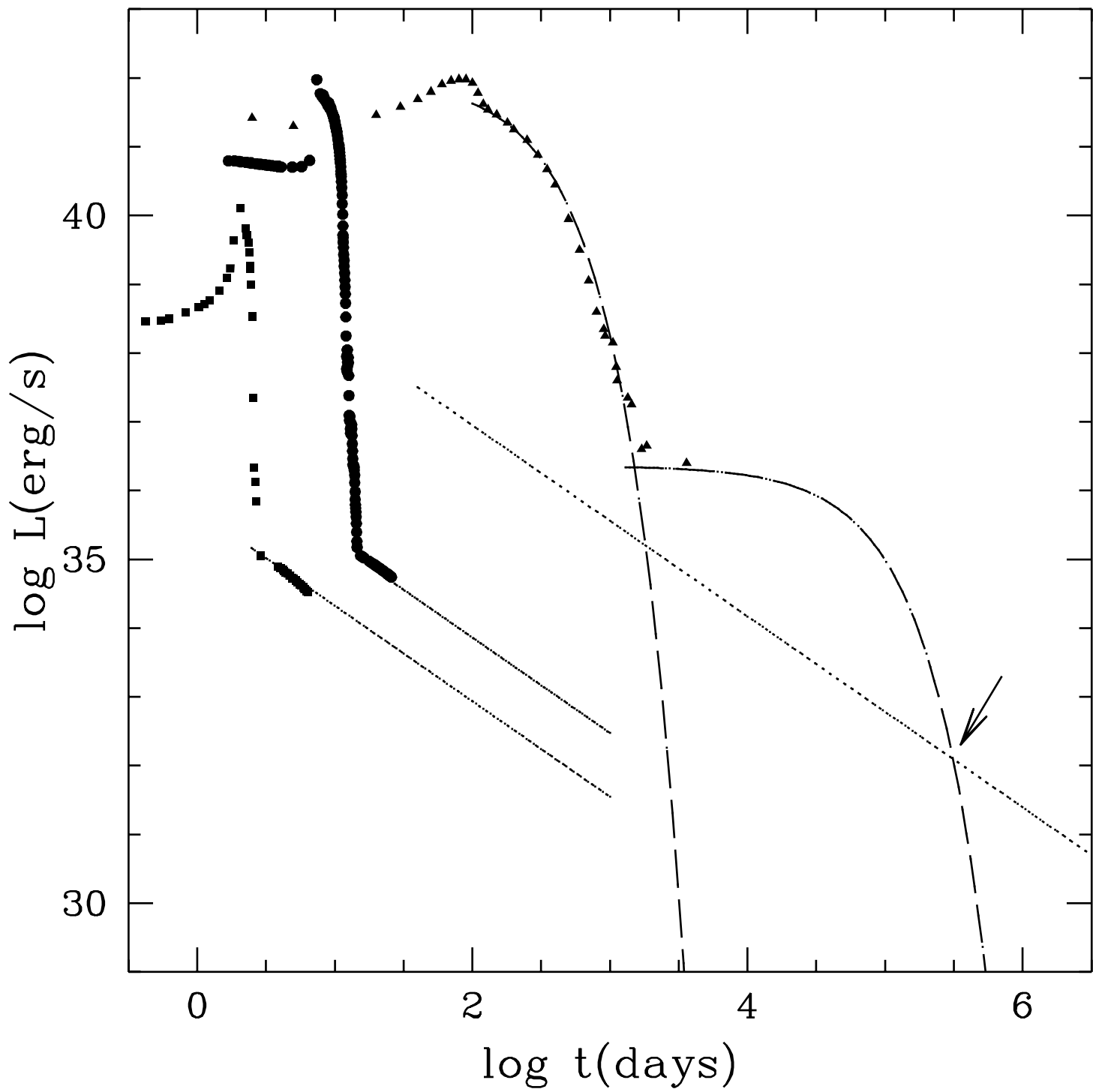


TABLE 1

PARAMETERS FOR THE COMPUTED MODELS

model	\tilde{k}^a	$c_{s,0}$ (cm s $^{-1}$)	M_{cloud} (M_\odot)	r_{out} (cm)	V_0^b (cm s $^{-1}$)	ρ_0^c (g cm $^{-3}$)	T_0^d (K)	$t_{a,0}^e$	t_0^f	t_{diff}^g	t_{trans}^h	t_{rec}^i
I	1	3.5×10^7	10^{-5}	3×10^{12}	6.4×10^8	1.8×10^{-10}	9×10^4	1.3 h	1.3 h	1.6 h	19 h	∞
II	1	3.5×10^7	10^{-2}	3×10^{12}	6.4×10^8	1.8×10^{-7}	5×10^5	1.3 h	1.3 h	2.1 d	25 d	∞
III	0.1	3.5×10^7	10^{-2}	3×10^{12}	6.4×10^7	1.8×10^{-7}	5×10^5	1.3 h	13 h	6.7 d	250 d	∞
IVa	1	3.5×10^7	10^{-2}	3×10^{12}	6.4×10^8	1.8×10^{-7}	5×10^5	1.3 h	1.3 h	2.1 d	25 d	2.7 d
IVb	0.1	10^8	1	3×10^{12}	1.5×10^9	1.8×10^{-5}	2.7×10^6	0.055 h	0.55 h	14 d	107 d	6.2 d

^a $\tilde{k} = t_{a,0}/t_0$.

^bExpansion velocity of the outermost shell.

^cDensity of the cloud at the onset of homologous expansion.

^dInitial temperature in the inner part of the cloud.

^eAccretion timescale (equation [33]).

^fExpansion timescale (equation [34]).

^gDiffusion timescale (equation [35]).

^hThick–thin transition timescale (equation [36]).

ⁱRecombination timescale (equation [37]).

NOTE.—The mass of the black hole is taken to be $M_{bh} = 1.5M_\odot$.

TABLE 2
PARAMETERS OF SN1987A

\tilde{k}^a	$c_{s,0}$ (cm s ⁻¹)	M_{cloud} (M_{\odot})	r_{out} (cm)	V_0^b (cm s ⁻¹)	ρ_0^c (g cm ⁻³)	T_0^d (K)	$t_{a,0}^e$	t_0^f	t_{diff}^g	t_{trans}^h	t_{rec}^i
Parameters for the hydrogen envelope (taken from Arnett 1996)											
0.0067	1.6×10^8	15	3×10^{12}	4×10^8	2.7×10^{-4}	6.7×10^6	0.014 h	2.1 h	103 d	4.2 y	58 d
Parameters for the mantle (taken from Chevalier 1989)											
0.66	3.5×10^7	4	9×10^{11}	1×10^8	3×10^{-3}	5.7×10^6	1.3 h	2 h	107 d	6.2 y	110 d